Mode-{I, III} multiaxial fatigue of welded joints in steel maritime structures

Effective notch stress based resistance incorporating strength and mechanism contributions

Bufalari, Gabriele; den Besten, Henk; Kaminski, Miroslaw Lech

DOI
10.1016/j.ijfatigue.2023.108067

Publication date
2024

Document Version
Final published version

Published in
International Journal of Fatigue

International Journal of Fatigue 180 (2024) 108067

Contents lists available at ScienceDirect

International Journal of Fatigue

journal homepage: www.elsevier.com/locate/ijfatigue

Mode-{I, III} multiaxial fatigue of welded joints in steel maritime structures: Effective notch stress based resistance incorporating strength and mechanism contributions

Gabriele Bufalari, Henk den Besten *, Miroslaw Lech Kaminski

Maritime and Transport Technology Department, Delft University of Technology, Delft, The Netherlands

ARTICLE INFO

Keywords:
Fatigue
Multiaxiality
Welded joints
Strength and mechanism
Effective notch stress

ABSTRACT

The response of maritime structures can be multiaxial, involving predominant mode-I and non-negligible mode-III components. Adopting a stress distribution formulation based effective notch stress as fatigue strength parameter for mixed mode-{I, III} multiaxial fatigue assessment purposes, a mode-I equivalent von Mises type of failure criterion has been established at the critical fracture plane. Counting includes a cycle-by-cycle non-proportionality measure and damage accumulation is based on a linear model. Distinguished mode specific and material characteristic strength and mechanism contributions in terms of respectively the resistance curve intercept and mean stress induced response ratio coefficient, resistance curve slope and material characteristic length, have been incorporated. Evaluating the mid-cycle fatigue resistance, the outperformance is impressive. The analysed multiaxial mode-{I, III} data fits the uniaxial mode-I reference data scatter band and a single resistance curve can be used for fatigue assessment.

1. Introduction

Maritime structures are typically exposed to environment and service induced loading conditions varying over time, introducing a cyclic response. Fatigue can be a governing limit state [1]. For commonly applied materials like steel, the arc-welded joints typically connecting the planar or tubular structural members are fatigue sensitive because of the notched geometries; hot spots [2].

In general, maritime structural response conditions can be multiaxial with potential contributions from loading, geometry and/or even material sources. External environment and service loading components, like wind and waves from different directions, as well as heavy lifting operations and rotating turbine blades (Fig. 1), can occur simultaneously. Stiffness variations because of changing geometry or material anisotropy enable multiple – internal – load transfer mechanisms along dissimilar paths. Normal mode-I, in-plane shear mode-II and/or out-of-plane mode-III shear components (Fig. 2) can be involved, either proportional (P); i.e. in-phase (predominantly geometry and material source related), or non-proportional (NP); i.e. out-of-phase (often related to the loading source) because of asynchronous behaviour and/or different frequencies [3].

Since the (curved) plate thickness is often relatively small in comparison to the other structural member dimensions and the external loading is typically a distributed one, the internal mode-I loading components: normal force F_n as well as the in-plane and out-of-plane bending moments $M_{b,ip}$ and $M_{b,op}$, are typically governing. Any in-plane shear force $F_{s,ip}$ mode-II component is in general negligibly small. At the same time, the out-of-plane shear force $F_{s,op}$ and torsion moment M_t mode-III components affect in specific cases [4,5] the predominant mode-I response and multiaxiality has to be taken into account for accurate fatigue strength and life time estimates [e.g. 3]. Adopting respectively intact and cracked geometry parameters [2], the initiation and growth contributions to the fatigue damage process can be modelled [1]. The fatigue life time N is predominantly spent in the notch affected region [6], meaning a notch characteristic intact geometry parameter can be adopted as fatigue strength parameter S rather than a cracked geometry one, even if N for welded joints is typically crack growth defined. Since far field response spectra of welded joints in steel maritime structures reflect predominantly linear elastic behaviour, S is typically of the stress – rather than strain or energy – type, in particular for mid- and high-cycle fatigue [7]. Correlation of S and N typically reveals a log–log linear dependency and a Basquin type of resistance relation is naturally adopted: $\log(N) = \log(C) - m \cdot \log(S)$. Intercept $\log(C)$ and slope m reflect respectively a strength and mechanism contribution, suggesting the mode-I and mode-III values are different.

Different fatigue strength parameters have been developed over time aiming to obtain more accurate lifetime estimates, balanced with

* Corresponding author.
E-mail address: henk.denbesten@tudelft.nl (H. den Besten).

https://doi.org/10.1016/j.ijfatigue.2023.108067
Received 25 September 2023; Received in revised form 30 October 2023; Accepted 18 November 2023
Available online 22 November 2023

Nomenclature

Symbols

α	(half) notch angle
β_a	particular stress angle
$\beta(N)$	lifetime dependent shear strength coefficient
γ	response ratio coefficient
Δ	prefix indicating stress range
ϵ	residual
$\{\zeta_{\sigma a}, \zeta_{\sigma s}\}$	mode-I blunt body eigenvalue of (anti-)symm. part
θ	generic (stress) angle
λ	eigenvalue
$\{\lambda_{\sigma a}, \lambda_{\sigma s}\}$	mode-I eigenvalue of (anti-)symmetry part
λ_τ	mode-III eigenvalue
$\{\mu_{\sigma a}, \mu_{\sigma s}\}$	mode-I equilibrium coeff. of (anti-)symmetry part
$\mu_{\tau F}$	mode-III force equilibrium coefficient
$\mu_{\tau M}$	mode-III moment equilibrium coefficient
ρ	(real) weld notch radius
ρ_{S_∞}	mid/high-cycle fatigue transition curvature
ρ^*	material characteristic length
ρ_τ	normal to shear stress ratio
σ	normal stress
σ_e	mode-I effective notch stress
σ_{fe}	mode-I linear structural field stress
σ_N	fatigue lifetime standard deviation
$\sigma_n\ (r/t_p)$	weld toe notch normal stress distribution
σ_s	(structural) normal stress
σ_{se}	mode-I self equilibrium stress
σ_{sb}	M_b induced structural normal stress component
σ_{sm}	F_n induced structural normal stress component
σ_y	material yield strength
τ	shear stress
τ_e	mode-III effective notch stress
τ_{fe}	mode-III linear structural field stress
$\tau_n\ (r/t_p)$	weld toe notch shear stress distribution
τ_s	(structural) shear stress
τ_{se}	mode-III self equilibrium stress
τ_{ss}	F_s induced structural shear stress component
τ_{st}	M_t induced structural shear stress component
Φ	parameter vector
$\{\chi_{\sigma a}, \chi_{\sigma s}\}$	mode-I eigenvalue coeff. of $\{\lambda_{\sigma a}, \lambda_{\sigma s}\}$
$\{\omega_{\sigma a}, \omega_{\sigma s}\}$	mode-I blunt body eigenvalue coeff. of $\{\zeta_{\sigma a}, \zeta_{\sigma s}\}$
C	fatigue resistance curve intercept
C_{bw}	weld load carrying normal stress coefficient
C_{np}	path characteristic non-proportionality coefficient
c_m	material characteristic non-proportionality coeff.
C_{tw}	weld load carrying shear stress coefficient
F_n	nodal normal force
F_s	nodal shear force
h_w	weld leg height
l_w	weld leg length
m	fatigue resistance curve slope
M_b	nodal bending moment
M_t	nodal torsion moment
n	number of counted cycles
N	fatigue lifetime in number of cycles
p_s	probability of survival
r_0	radial distance coordinate system origin to notch tip
r	radial coordinate
r_{σ_s}	structural normal stress ratio
r_{τ_s}	structural shear stress ratio
R	response ratio
R_r	response ratio including S_r
R_t	tube outer radius
S	fatigue strength parameter
S_r	(mean) residual stress
S_e	effective notch stress parameter
S_∞	fatigue strength limit
t_b	base plate thickness
t_c	cross plate thickness
t_p	plate thickness
$T_{\sigma S}$	10% – 90% strength scatter band index
$\mathcal{L}$	log-likelihood
$_I$	mode-I index
$_{III}$	mode-III index

Abbreviations

AW	as-welded
CA	constant amplitude
DS	double side
FE	finite element
MLE	maximum likelihood estimate
NP	non-proportional
P	proportional
SR	stress-relieved
SS	single side
VA	variable amplitude
VAR	variance

parameter complexity and computational efforts [8]. Incorporating local (notch) information provides more generalized S formulations and the number of involved fatigue resistance curves reduces accordingly (i.e. ultimately to one), like for the effective notch stress concept [8–14]. Embedded in the critical distance theory [15], applications are not limited to welded joints but extents for example to 3D printed materials and structures [16–19]. Taking advantage of semi-analytical weld notch stress distribution expressions [8,20], the effective notch stress S_e can be calculated averaging the notch stress distribution along the expected crack path over a material characteristic length ρ^*, introducing another mechanism contribution. Solid finite element (FE) models to estimate S_e are not required anymore. Uniaxial mode-I and mode-III investigations revealed distinguished $\{\rho^*_I, \rho^*_{III}\}$ as well as $\{\log(C_I), \log(C_{III})\}$ and $\{m_I, m_{III}\}$ values [7,8,20]. Since a response cycle needs two parameters for a complete spatial description, e.g. range and ratio, mode specific response ratio coefficients $\{\gamma_I, \gamma_{III}\}$ containing another strength contribution have been proposed as well [7,8,20]. However, consequences for mode-{I, III} multiaxial fatigue have not been investigated before.

Fig. 1. Support vessel and wind turbine, resp. a planar and tubular maritime structure.

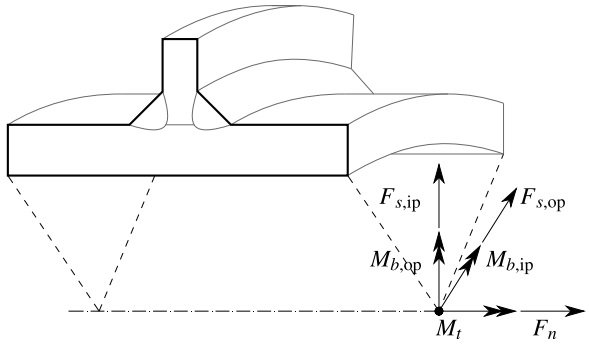

Fig. 2. DS welded T-joint in a tubular structure with internal load components.

Aiming to reduce the still relatively large multiaxial fatigue resistance scatter [e.g. 21,22], dedicated mode-{I, III} strength and mechanism related contributions, respectively $\{\log(C), \gamma\}$ and $\{m, \rho^*\}$, will be incorporated in order to obtain improved lifetime estimates. An S_e based multiaxial fatigue strength parameter will be established considering all relevant assessment aspects for a time domain approach (Section 2) and the performance will be evaluated using multiaxial fatigue resistance data (Section 3).

2. Multiaxial fatigue aspects

Based on fatigue damage criteria classification [2], particular attention will be paid first to modelling aspects for different types of criteria, looking at static and fatigue strength similarities, as well as differences between infinite and finite life criteria (Section 2.1). In order to be able to deal with random multiaxial response conditions, damage plane selection (Section 2.2) and cycle counting aspects will be addressed (Section 2.3), including ways to deal with non-proportionality (Section 2.4). Last but not least, fatigue damage accumulation model considerations will be discussed (Section 2.5).

2.1. Failure criterion

Classical failure criteria for more ductile isotropic materials, including polycrystalline metals like steel, already aim to estimate yielding of materials for monotonic – ultimate strength related – multiaxial response (i.e. stress) conditions [23].

Any stress tensor can be decomposed into the sum of a hydrostatic (mean) and deviatoric (shear induced) part. Whereas the hydrostatic part introduces a volume change only without deformation, the deviatoric one is associated with shape change, distortion. Polycrystalline metals comprise of grains with different shape, size and orientation, meaning for any loading condition each grain shows a different amount of slip; a shear induced response, changing the shape. After failure, slip bands turn out to be visible at the fracture surface, i.e. experimental evidence suggesting the Tresca maximum shear stress criterion is decisive [24]. For shell/plate type of structures only the mode-III component is relevant: $S = \max(\tau_{III}) \leq \sigma_y$, since the mode-II contribution is negligible. At the same time, experimental evidence shows that ductile materials do not fail in case of a hydrostatic stress component only (e.g. metals in deep ocean waters), introducing the distortion based von Mises maximum deviatoric stress criterion [24]. For shell/plate type of structures principally containing a governing mode-I normal and mode-III shear component only: $S = \max\left\{\sqrt{\sigma_I^2 + \beta \cdot \tau_{III}^2}\right\} \leq \sigma_y$. The von Mises criterion is essentially an equivalent normal stress formulation. Shear strength coefficient β is a material constant. For steel $\beta = 3$ is typically adopted [24].

For cyclic – fatigue strength related – multiaxial response conditions, linear and non-linear failure criteria have been proposed for the infinite life region [e.g. 25–27]. A fatigue resistance limit is naturally introduced, defining the threshold for an unlimited number of cycles: $S_\infty(N \to \infty)$. Based on different modelling philosophies, the criteria are principally a combination of two parameters: a primary governing term and a secondary correcting one. The linear criteria: $S = \max\{C_1 \cdot f(S_1) + C_2 \cdot g(S_2)\} \leq S_\infty(N \to \infty)$, seem of the Tresca type; the non-linear ones: $S = \max\{\sqrt{C_1 \cdot f(S_1)^2 + C_2 \cdot g(S_2)^2}\} \leq S_\infty(N \to \infty)$, of the von Mises type. Parameters S_1 and S_2 are for example the deviatoric and (max) hydrostatic stress, respectively, taking the complete stress state into account. The shear stress – assuming crack initiation provides the major contribution to the fatigue lifetime – and (max) hydrostatic stress can be used as well. Alternatively, the shear stress τ_{III} and (max) normal stress σ_I are adopted [e.g. 28], reflecting the multiaxial mode-I and mode-III contributions. Constants C_1 and C_2 are (fitted) material dependent coefficients. Since a response cycle requires two parameters for a complete definition in space, e.g. the stress range S and the response ratio $R = S_{min}/S_{max}$, both may affect the fatigue strength and the criteria may even turn into: $S = \max\{C_1 \cdot f(S_1, R_1) + C_2 \cdot g(S_2, R_2)\} \leq S_\infty(N \to \infty)$ for an equivalent shear stress and $S = \max\{\sqrt{C_1 \cdot f(S_1, R_1)^2 + C_2 \cdot g(S_2, R_2)^2}\} \leq S_\infty(N \to \infty)$ for an equivalent normal one.

For the finite life region, principally the same type of criteria could be adopted, although the coefficients will become response level dependent and the fatigue limit will turn into a lifetime dependent fatigue resistance relation because of the finite number of response cycles N: $S = \max\{C_1(S_1) \cdot f(S_1, R_1) + C_2(S_2) \cdot g(S_2, R_2)\} \leq S(N)$ and $S = \max\{\sqrt{C_1(S_1) \cdot f(S_1, R_1)^2 + C_2(S_2) \cdot g(S_2, R_2)^2}\} \leq S(N)$. The governing mode-I and mode-III log–log linear mid-cycle fatigue resistance relations (Fig. 3): $\log(N) = \log(C) - m \cdot \log(S) \to \log(S) = \{\log(C) - \log(N)\}/m \to S(N) = (N/C)^{-1/m}$, have characteristic intercept and slope parameters $\{\log(C), m\}$, respectively reflecting different fatigue strengths and mechanisms. In case initiation dominates the fatigue lifetime, the shear stress is in control and a Tresca type of criterion seems straightforward. If growth provides the major contribution, an equivalent normal stress based von Mises type of criterion makes sense.

Adopting an (equivalent) shear stress $S = \max[\mathrm{VAR}\{\tau_{III}(t)\}]$ based on a primary governing term only, a response based normal to shear stress ratio has been introduced to establish the failure criterion [21, 29–31]: $\rho_\tau = \Delta\sigma_I/\Delta\tau_{III} = \sqrt{[2 \cdot \mathrm{VAR}\{\sigma_I(t)\}]}/\sqrt{[2 \cdot \mathrm{VAR}\{\tau_{III}(t)\}]}$. Incorporating the relative mode-I and mode-III contributions, a response representative – rather than mode-III equivalent – resistance curve has been proposed with $\log\{C(\rho_\tau)\} = a \cdot \rho_\tau + b$ and $m(\rho_\tau) = c \cdot \rho_\tau + d$, turning the criterion into: $S = \max[\mathrm{VAR}\{\tau_{III}(t)\}] \leq \{N/C(\rho_\tau)\}^{-1/m(\rho_\tau)}$. Coefficients $\{a, b, c, d\}$ are based on the mode-I and mode-III reference resistance curve parameters. Since both the resistance and response information define $[\log\{C(\rho_\tau)\}, m(\rho_\tau)]$, the intercept and slope can become out of (resistance) control. Bounds have been provided [31, 32], but remain a modelling limitation. Involving the mean stress as a 2nd parameter to define a cycle in space, the equivalent shear

stress turns into an effective one [30]: $S = \max[\mathrm{VAR}\{\tau_{III}(t)\}_{eff}] \leq \{N/C(\rho_\tau)\}^{-1/m(\rho_\tau)}$. A similar ratio has been proposed to establish a shear stress fitting coefficient $C_2\{\Delta\tau_{III}/\Delta\sigma_I\}$, aiming to obtain a mode-III equivalent resistance curve [33]. Explicit model limitations do not seem to exist, although the multiaxial test data fitted $C_2(\Delta\tau_{III}/\Delta\sigma_I)$ formulation implicitly determines up to what extent the criterion: $S = \max[S_1 + C_2\{\Delta\tau_{III}/\Delta\sigma_I\} \cdot S_2] \leq \{N/C_{III}\}^{-1/m_{III}}$ with $S_1 = \Delta\tau_{III}$ and $S_2 = \Delta\sigma_I$, is applicable.

For a finite lifetime, the ratio of the mode-I and mode-III fatigue strength depends on the number of cycles N until failure (Fig. 3), meaning that for an equivalent normal stress criterion the shear strength coefficient has to be response level dependent rather than constant [e.g. 28]: $S = \max[\sqrt{\sigma_I^2 + \beta\{\sigma_I(N), \tau_{III}(N)\} \cdot \tau_{III}^2}]$, with $\beta = \Delta\sigma_I(N)/\Delta\tau_{III}(N) = C \cdot N^M$, $C = 10^{\{m_{III}\cdot\log(C_I) - m_I\cdot\log(C_{III})\}/\{m_I \cdot m_{III}\}}$ and $M = (m_I - m_{III})/(m_I \cdot m_{III})$. Both uniaxial and multiaxial mode-{I, III} fatigue test data should fit in the mode-I resistance data scatter band, reflecting the same equivalent strength and mechanism, i.e. intercept and slope: $S = \max[\sqrt{\sigma_I^2 + \beta\{\sigma_I(N), \tau_{III}(N)\} \cdot \tau_{III}^2}] \leq \{N/C_I\}^{-1/m_I}$. The $S(N)$ formulation is fully resistance defined and $\beta(\sigma_I, \tau_{III})$ bounds, either real or artificial, are not required.

Although the shear strength coefficient should be response level dependent, still a constant β has been used since the fatigue resistance data scatter would hardly reduce [34,35]. However, at least the uniaxial mode-I and mode-III data is not aligned since the mode-III data is mode-I equivalent at one particular number of cycles only, rather than over the full finite lifetime range. Hardly observing a reduction in fatigue resistance scatter seems a consequence of unbalanced uniaxial mode-I, mode-III and multiaxial mode-{I, III} data in general, or at least ignoring the resistance characteristics for the particular groups of data. Adopting a constant β, regression analysis will principally provide biased, i.e. averaged, fatigue strength and damage mechanism contributions with respect to $\{\log(C), m\}$. In case the mode-I parameters are simply adopted, the mode-III contribution is not properly taken into account. A mean stress correction is typically limited to a mode-I contribution, introducing an effective normal stress $\sigma_{I,eff}$ [e.g. 28,36].

Rather than a resistance based shear strength coefficient, a response dependent one: $\beta(\Delta\sigma_I, \Delta\tau_{III})$ — similar to the normal to shear stress ratio ρ_τ for the equivalent shear stress criterion, has been proposed [21,37–39]. The uniaxial mode-I and mode-III reference conditions can be represented, although for a multiaxial response $\beta(\Delta\sigma_I, \Delta\tau_{III})$ can take unrealistic values since fatigue resistance related limitations are lacking.

2.2. Damage plane

Whereas for proportional (i.e. in-phase) multiaxial mode-{I, III} response conditions in a particular 2D $\{S_1, S_2\}$- plane with angle ϕ only

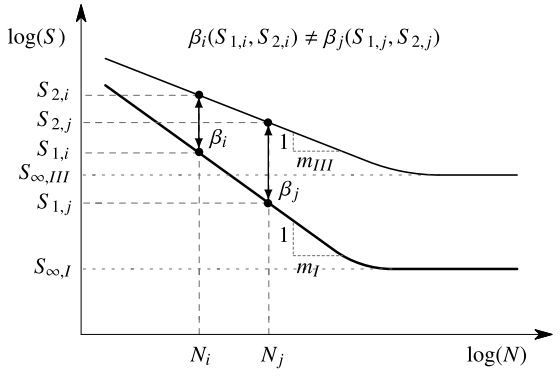

Fig. 3. Lifetime dependent mode-I and mode-III fatigue strength ratio.

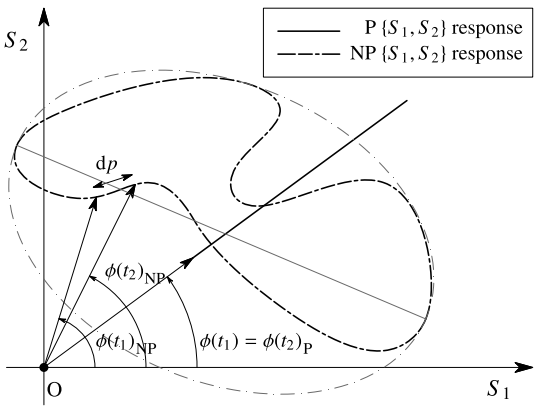

Fig. 4. Temporal evolution of stress in the $\{S_1, S_2\}$- stress plane.

the stress tensor magnitude is changing (Fig. 4), the tensor additionally rotates for non-proportional (i.e. out-of-phase) ones and the plane angle $\phi(t)$ is varying in time.

Incorporating the damage contribution of all planes explicitly introduces typically an equivalent fatigue strength parameter: $S_{eq} = (1/2\pi) \cdot \int S(\phi)\mathrm{d}\phi$, representing the integral plane [e.g. 37,38,40]. Alternatively, an enclosing surface like an ellipse can be established in the von Mises stress plane based on the perimeter p (Fig. 4) — an implicit angle measure, meaning: $S_{eq} = (1/p) \cdot \int S(p)\mathrm{d}p$ [e.g. 41].

Rather than the integral plane, only the governing, i.e. critical plane can be considered, e.g. based on the maximum value of the adopted fatigue strength parameter S, either an equivalent shear stress [e.g. 29–31]: $S = \max[\mathrm{VAR}\{\tau_{III}(\phi)\}]$, or an equivalent normal one [e.g. 28,41,42]: $S = \max[\sqrt{\sigma_{I,max}^2(\phi) + \beta\{\sigma_I(N), \tau_{III}(N)\} \cdot \Delta\tau_{III}^2(\phi)}]$. Since the stiffness distribution of (maritime) structures in stiffened panel configuration is predominantly orthotropic and cracks at the weld notches typically develop first in plate thickness direction, the fracture plane can be used as well to obtain S [e.g. 34].

The full stress tensor of a volume element consists of 3 normal- and 6 shear stress components. For (quasi) isotropic materials (like steel) in static equilibrium, element rotation is prevented for and tensor symmetry appears: $\tau_{ij} = \tau_{ji}$, reducing the tensor content to 3 normal- and 3 shear stress components only. Certain symmetric stress tensor properties are coordinate system rotation (i.e. plane) independent, introducing invariants. Both tensor parts (Section 2.1) can be incorporated in terms of invariants to take the complete stress state into account [e.g. 40,43]. The hydrostatic part, equal to one third of the first tensor invariant I_1, is basically the average normal stress; a mean value. The square root of the second invariant of the deviatoric stress $\sqrt{J_2}$ represents the other part, often incorporated as a von Mises type of criterion: $\sqrt{\beta \cdot J_2}$; a stress range, with the shear stress coefficient β either constant or response level dependent. Both invariants represent up to some extent 2 parameters defining a cycle in space.

2.3. Cycle counting

Although for a mode-I or mode-III uniaxial response cycle counting – i.e. identification of the number of closed hysteresis loops – is principally required for variable amplitude (VA) conditions, in case of a mode-{I- III} multiaxial one cycle counting can already be relevant for constant amplitude (CA) conditions, in particular when asynchronous behaviour is involved and/or the frequencies are different. However, if multiaxial cycle counting is required, depends on the adopted failure criterion (Section 2.1) and selected damage plane (Section 2.2).

For an equivalent fatigue strength parameter $S_{eq}(t)$ at the integral plane — either of the Tresca or von Mises type, at each time instant

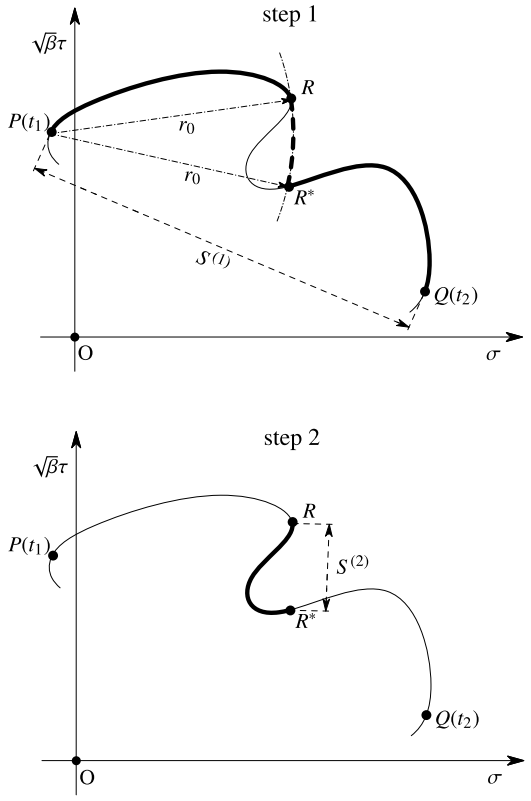

Fig. 5. Cycle counting illustration in the von Mises plane, searching for the max. range [e.g. 34,35,48–50].

$S_{eq}(t)$ can be established. Reducing the time series to a peak–valley sequence, uniaxial (rain flow) counting can be adopted in order to obtain the equivalent stress spectrum $\{S_{eq}(n)\}$ [e.g. 38].

In case of a Tresca type of criterion at the critical plane, $S(t)$ can still be processed using uniaxial rain flow counting [e.g. 31]. Virtual cycles have been counted based on zero crossings [44], rather than closed hysteresis loop criteria, but suggest at least that mean stress effects cannot be incorporated. Adopting a von Mises type of criterion, several ways of cycle counting have been considered. The uniaxial rain flow counting algorithm can be straightforward applied to $S(t)$, but sign information – lost by definition – should be incorporated [e.g. 45,46]. However, sign changes may cause artificial anomalies affecting the von Mises time series and providing unrealistic counting results. Introducing a primary and secondary channel, multiaxial rain flow counting has been proposed. In fact, one von Mises stress component is counted (e.g. the mode-I normal stress) at the primary channel and the corresponding other one (e.g. the mode-III shear stress) at the secondary channel is a projection at the primary channel peak–valley location [e.g. 47]. Although at least the mode-I and mode-III components have been incorporated up to some extent, the established cycles are not likely multiaxial closed hysteresis loops. However, an algorithm continuously searching for the maximum range in the time series (segments) at the von Mises plane (Fig. 5) provides cycles reflecting closed hysteresis loops [e.g. 34,35,48–50]. In case the structural response is uniaxial, the results are the same as obtained with rain flow counting.

If in terms of invariants only the damage related tensor component, i.e. the deviator, is involved, uniaxial rain flow counting is straightforward applied. When the hydrostatic component is involved as well, multiaxial rain flow counting can be used adopting a primary and secondary channel [e.g. 43].

2.4. Non-proportionality

The normal mode-I and shear mode-III stress components are not necessarily proportional, e.g. because of asynchronous behavour, different frequencies or time varying amplitudes. How non-proportionality is incorporated typically depends on the adopted type of criterion (Section 2.1), selected damage plane (Section 2.2) and cycle counting procedure (Section 2.3).

Since an equivalent fatigue strength parameter (Section 2.2) takes the damage contribution of all planes into account, any type of non-proportionality is principally incorporated in the criterion. Adopting for example a von Mises type of criterion; an equivalent normal stress, non-proportionality is considered introducing a shear stress variations $\tau(\phi)$ based correction: $S_{eq} = S(\phi = 0) \cdot f\{\tau(\phi)\}$, assuming $\tau(\phi)$ to be the basic requirement to develop fatigue damage [37,38].

Although for an equivalent shear stress like $S = \max[\mathrm{VAR}\{\tau_{III}(t)\}]$ [31] the normal stress component is not explicitly considered, the response based normal to shear stress ratio $\rho_\tau = \Delta\sigma_I/\Delta\tau_{III} = \sqrt{[2 \cdot \mathrm{VAR}\{\sigma_I(t)\}]}/\sqrt{[2 \cdot \mathrm{VAR}\{\tau_{III}(t)\}]}$ defining the characteristic resistance curve incorporates at least an average non-proportionality measure. Using a similar ratio $C_2\{\tau(t)/\sigma(t)\}$, the equivalent shear stress takes the instantaneous $\{\sigma(t), \tau(t)\}$ contributions into account, meaning non-proportionality is explicitly considered: $S = [S_1 + C_2\{\tau(t)/\sigma(t)\} \cdot S_2]$ with $S_1 = \tau(t)$ and $S_2 = \sigma(t)$ [44].

For an equivalent normal stress of the von Mises type at the critical plane, non-proportionality can be considered in different ways. Using the instantaneous normal and shear stress contributions $\{\sigma(t), \tau(t)\}$, non-proportionality is explicitly incorporated. Even if only a single component has been counted (e.g. the mode-I normal stress) at the primary channel and the corresponding other one (e.g. the mode-III shear stress) at the secondary channel is a projection at the primary channel peak–valley location, meaning the non-proportional time series are basically turned into quasi-proportional ones, non-proportionality is implicitly included up to some extent [e.g. 47]. Cycle counting in the von Mises stress (critical) plane (Section 2.3) allows to capture at least the stress range. However, the actual response path or perimeter has been identified as being crucial (Fig. 6). Introducing an effective stress range $S_{eff} = S(1 + c_m \cdot C_{np})$, with $C_{np} = \int_{\widetilde{S}}\{r \cdot |\sin(\theta)|\}^n \mathrm{d}p / \int_S\{R \cdot |\sin(\theta)|\}^n \mathrm{d}p$ and $n = \{0, 1, 2\}$ for respectively either a 0^{th} order moment (representing length), 1^{st} order (static) moment or 2^{nd} order moment (of inertia) based path correction factor incorporating the level of non-proportionality for each cycle relative to the straight line defined stress range (Fig. 6). Any material characteristic non-proportionality effect is reflected in fitting coefficient c_m [34,35,49,50].

Adopting a failure criterion based on the full stress tensor, multiaxial rain flow counting of the invariants $\sqrt{J_2}$ or $\sqrt{\beta \cdot J_2}$ and the projection of the corresponding I_1 at respectively the primary and

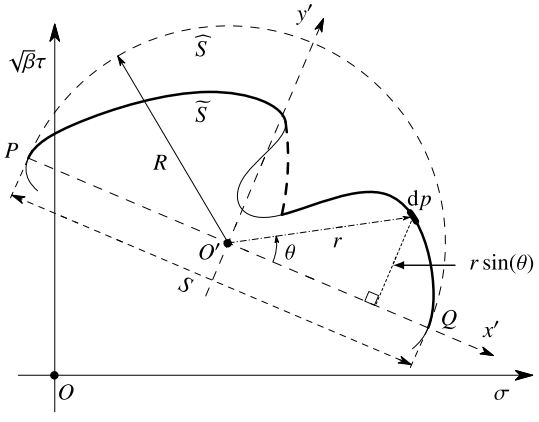

Fig. 6. Cycle-by-cycle response path based non-proportionality in the von Mises plane.

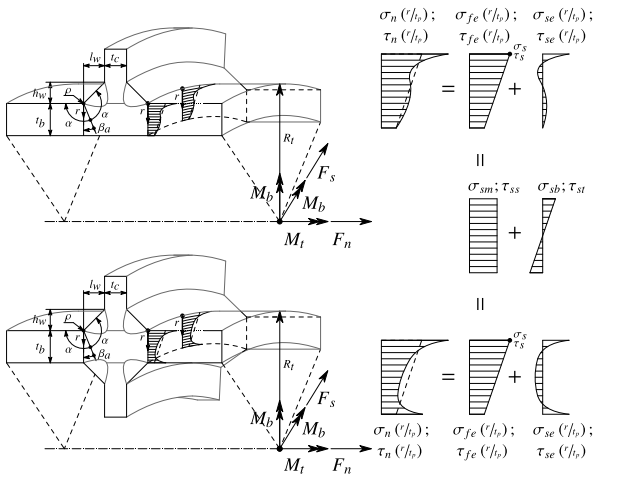

Fig. 7. Linear superposition of an equilibrium equivalent and self-equilibrium part for the mode-{I, III} weld toe notch shear stress distribution of a DS welded T-joint and DS welded cruciform joint in a tubular structure.

secondary channel [43] implicitly includes non-proportionality up to some extent.

2.5. Damage accumulation

Fatigue damage is progressive and accumulates cycle-by-cycle, meaning history counts. Both linear and non-linear models have been developed over time [e.g. 51,52], although typically for uniaxial response conditions. Application extends to multiaxial ones as well, since the failure criteria are typically of the equivalent stress type (Section 2.1) and even multiaxial rain flow counting (Section 2.3) is limited to the primary channel, meaning a single time series is considered for damage accumulation.

The linear damage model $D = \sum\{n_i(S_i)/N_i(S_i)\} \leq 1$; the sum of the ratios of the number of response cycles at a particular level $n_i(S_i)$ and the corresponding resistance defined number of cycles to failure $N_i(S_i)$ [53,54], is the universal standard for fatigue design, as reflected in applications for criteria defined at the integral plane [38], the critical plane [31,33,34] and the invariant plane [43].

However, numerous test results have shown the deficiency, including possible non-conservative D estimates [e.g. 52]. Sequence effects turned out to be an important one from response perspective and D for example proved to be different for a single overload in comparison to a single underload and for a low-to-high sequence different from a high-to-low one [e.g. 55]. Even for random response conditions as typically observed for a wave loading induced response of maritime structures, $D \neq 1$ is obtained for different types of spectra [e.g. 56–59]. From resistance perspective, cycles with a stress range below the (random) fatigue limit affect D as well [e.g. 60]. Still adopting the linear model, the maximum allowed damage is typically reduced to a value below one, depending on the variable amplitude response characteristics [e.g. 38].

Most non-linear models [e.g. 51,52] addressing the response aspects are basically of the type: $D = \sum[C_i \cdot \{n_i(S_i)/N_i(S_i)\}^{f(S_i)}] \leq 1$, considering the linear one as a special case for $C_i = f(S_i) = 1$. Simplifications typically concern a bi-linearization. Fitting coefficient C_i and fitting function $f(S_i)$ are meant to incorporate any material specific contribution as well. So far, applications for multiaxial fatigue seem limited, although a non-linear model of this type has been adopted for S defined at the critical plane [28,47].

Anyway, a generalized, all-encompassing model overall outperforming the linear one is not available yet [e.g. 52]. At the same time, the damage accumulation model performance seems related to the adopted fatigue strength criterion. For and advanced S formulation the linear model still proved to be sufficient since variable amplitude fatigue resistance data fits the constant amplitude data scatter band [34,55,61].

When both mid- and high-cycle fatigue are involved, a resistance induced damage accumulation non-linearity appears as well, because of the changing slope (i.e. changing mechanism) as reflected in the 2-slope resistance curve formulations [e.g. 7]. For a bi-linear one with a finite high-cycle fatigue slope, still $D = \sum\{n_i(S_i)/N_i(S_i)\} \leq 1$, but the resistance part involves different slope contributions m based on the number of cycles at the mid- to high-cycle fatigue transition N_t: $\log\{N_i(S_i)\} = \log(C) - m \cdot \log(S_i)$ with $m = m_{mid}$ for $N_i \leq N_t$ and $m = m_{high}$ for $N > N_t$ [52,62]. However, D estimates are quite often observed to be non-conservative [e.g. 63]. In case of an infinitely high-cycle fatigue slope, like for the generalized random fatigue limit formulation [7,55,64]: $\log N_i(S_i) = \log(C) - m \cdot \log(S_i) - \rho_{S_\infty} \cdot \log\{1 - S_\infty(\mu, \sigma; D)/S_i\}$, the fatigue limit S_∞ decreases for increasing D, meaning the damage accumulation calculation becomes an iterative process: $D = \sum\{n_i(S_i)/N_i(S_i; D)\} \leq 1$.

3. Effective notch stress assessment

For mixed mode-{I, III} multiaxial response conditions of planar and tubular maritime structures, the mode-I contribution is governing (Section 1), meaning the normal stress σ_I is predominant. At the same time, the fatigue lifetime of arc-welded joints is growth – rather than shear induced initiation – controlled because of the welding induced defects, explaining why an equivalent normal stress based von Mises type of failure criterion will be adopted (Section 2.1). Since cracks at weld notches typically develop first in plate thickness direction, the fracture plane is identified as the critical one and will be selected for criterion evaluation (Section 2.2). Cycles will be counted – because of the time domain approach – in the von Mises plane (Section 2.3), in order to be able to incorporate non-proportionality cycle-by-cycle (Section 2.4). The linear damage accumulation model will be used, since good performance has been shown for advanced fatigue strength criteria. Including a response related non-linearity may correct for fatigue strength parameter deficiencies because of the fitting involved, which should be identified first. Starting with mid-cycle fatigue, the resistance related non-linearity is not required as well (Section 2.5).

Opting for an effective notch stress based fatigue strength parameter, a failure criterion $S = S_e = \sqrt{\{ S_{e,I}^2 + \beta(N) \cdot S_{e,III}^2 \}}$ will be established first (Section 3.1) and includes a lifetime dependent shear stress coefficient $\beta(N)$. Using fatigue test data from literature (Section 3.2) the strength and mechanism contributions, reflected in respectively mode specific $\{\log(C), \gamma\}$ and $\{m, \rho^*\}$ coefficients, will be investigated (Section 3.3).

3.1. Fatigue strength parameter

The through-thickness weld notch stress distributions along the expected (2D) crack path – defining the fracture plane – are assumed to be a key element for an appropriate fatigue design and detectable repair criterion [8]. Semi-analytical formulations $\{\sigma_n(r/t_p), \tau_n(r/t_p)\}$, with plate thickness t_p either the base plate or cross plate value, t_b or t_c, have been developed for both non-symmetry and symmetry with respect to half the plate thickness ($t_p/2$), using respectively a double side (DS) welded T-joint and DS welded cruciform joint for illustration purposes (Fig. 7), in case of both zero and finite notch radius ρ [8,20]. Adopting a linear superposition principle [61], far field related equilibrium equivalent and self-equilibrium parts $\{\sigma_{fe}, \sigma_{se}; \tau_{fe}, \tau_{se}\}$ have been distinguished (Fig. 7), involving three components: the notch stress, the weld-load carrying stress and the far field stress. Typically three zones can be identified in all distributions: the zone 1 peak stress value, the zone 2 notch-affected stress gradient and the zone 3 far-field dominated stress gradient, demonstrating stress field similarity.

Since the (as) weld(ed) notch radius ρ is typically small, a zone 1 peak stress fatigue strength parameter would be too conservative.

Adopting a micro- and meso-structural notch support hypothesis, an effective notch stress estimate $\{\sigma_e, \tau_e\}$ has been obtained by averaging the notch stress distribution along the expected crack path over a material characteristic micro- and meso-structural length ρ^* – rather than introducing a fictitious notch radius, partially incorporating a zone 2 notch stress gradient – and zone 3 far field stress gradient contribution as well [34,43,65–69]. Physically speaking, ρ^* reflects the length in which the majority of the fatigue lifetime has been spent. For mode-I if $\rho = 0$ [8]:

$$\sigma_e = \frac{t_p}{\rho_I^*} \int_0^{\frac{\rho_I^*}{t_p}} \sigma_n \left(\frac{r}{t_p}\right) \mathrm{d}\left(\frac{r}{t_p}\right). \tag{1}$$

The effective notch stress parameter $S_{e,I} = \Delta\sigma_e$ becomes in case of non-symmetry with respect to $(t_p/2)$ [8,61]:

$$\begin{aligned} S_{e,\mathrm{I}} = \Delta\sigma_s \left(\frac{t_p}{\rho_\mathrm{I}^*}\right) \Bigg\{ & \frac{1}{\lambda_{\sigma s}} \left(\frac{\rho_\mathrm{I}^*}{t_p}\right)^{\lambda_{\sigma s}} \mu_{\sigma s}\lambda_{\sigma s}(\lambda_{\sigma s}+1)\cdot \\ & \left[\cos\{(\lambda_{\sigma s}+1)\beta_a\} - \chi_{\sigma s}\cos\{(\lambda_{\sigma s}-1)\beta_a\}\right] + \\ & \frac{1}{\lambda_{\sigma a}} \left(\frac{\rho_\mathrm{I}^*}{t_p}\right)^{\lambda_{\sigma a}} \mu_{\sigma a}\lambda_{\sigma a}(\lambda_{\sigma a}+1)\cdot \\ & \left[\sin\{(\lambda_{\sigma a}+1)\beta_a\} - \chi_{\sigma a}\sin\{(\lambda_{\sigma a}-1)\beta_a\}\right] + \\ & C_{bw}\left\{\left(\frac{\rho_\mathrm{I}^*}{t_p}\right)^2 - \left(\frac{\rho_\mathrm{I}^*}{t_p}\right)\right\} - r_{\sigma_s}\left(\frac{\rho_\mathrm{I}^*}{t_p}\right)^2 \Bigg\}. \end{aligned} \tag{2}$$

In case $\rho > 0$ and non-symmetry with respect to $(t_p/2)$ applies [8,61]:

$$\begin{aligned} S_{e,\mathrm{I}} = \Delta\sigma_s \left(\frac{t_p}{r_0+\rho_\mathrm{I}^*}\right) \Bigg\{ & \frac{1}{\lambda_{\sigma s}} \left[\left(\frac{r_0+\rho_\mathrm{I}^*}{t_p}\right)^{\lambda_{\sigma s}} - \left(\frac{r_0}{t_p}\right)^{\lambda_{\sigma s}}\right] \cdot \mu_{\sigma s}\lambda_{\sigma s}(\lambda_{\sigma s}+1)\cdot \\ & \left[\cos\{(\lambda_{\sigma s}+1)\beta_a\} - \chi_{\sigma s}\cos\{(\lambda_{\sigma s}-1)\beta_a\}\right] + \\ & \frac{1}{\zeta_{\sigma s}} \left[\left(\frac{r_0+\rho_\mathrm{I}^*}{t_p}\right)^{\zeta_{\sigma s}} - \left(\frac{r_0}{t_p}\right)^{\zeta_{\sigma s}}\right] \left(\frac{r_0}{t_p}\right)^{\lambda_{\sigma s}-\zeta_{\sigma s}} \lambda_{\sigma s} \frac{\left(\frac{2\alpha}{\pi}\right)}{4\left\{\left(\frac{2\alpha}{\pi}\right)-1\right\}} \cdot \\ & \left[\omega_{\sigma s1}\cos\{(\zeta_{\sigma s}+1)\beta_a\} + \omega_{\sigma s2}(\zeta_{\sigma s}+1)\cos\{(\zeta_{\sigma s}-1)\beta_a\}\right] + \\ & \frac{1}{\lambda_{\sigma a}} \left[\left(\frac{r_0+\rho_\mathrm{I}^*}{t_p}\right)^{\lambda_{\sigma a}} - \left(\frac{r_0}{t_p}\right)^{\lambda_{\sigma a}}\right] \mu_{\sigma a}\lambda_{\sigma a}(\lambda_{\sigma a}+1)\cdot \\ & \left[\sin\{(\lambda_{\sigma a}+1)\beta_a\} - \chi_{\sigma a}\sin\{(\lambda_{\sigma a}-1)\beta_a\}\right] + \\ & \frac{1}{\zeta_{\sigma a}} \left[\left(\frac{r_0+\rho_\mathrm{I}^*}{t_p}\right)^{\zeta_{\sigma a}} - \left(\frac{r_0}{t_p}\right)^{\zeta_{\sigma a}}\right] \left(\frac{r_0}{t_p}\right)^{\lambda_{\sigma a}-\zeta_{\sigma a}} \frac{\lambda_{\sigma a}}{4(\zeta_{\sigma a}-1)} \cdot \\ & \left[\omega_{\sigma a1}\sin\{(\zeta_{\sigma a}+1)\beta_a\} + \omega_{\sigma a2}(\zeta_{\sigma a}+1)\sin\{(\zeta_{\sigma a}-1)\beta_a\}\right] + \\ & C_{bw}\left\{\left(\frac{r_0+\rho_\mathrm{I}^*}{t_p}\right)^2 - \left(\frac{r_0}{t_p}\right)^2 - \left(\frac{2r_0+\rho_\mathrm{I}^*}{t_p}\right)\right\} - \\ & r_{\sigma_s}\left[\left(\frac{r_0+\rho_\mathrm{I}^*}{t_p}\right)^2 - \left(\frac{r_0}{t_p}\right)^2\right] \Bigg\}. \end{aligned} \tag{3}$$

For mode-III if $\rho = 0$ [20]:

$$\tau_e = \frac{t_p}{\rho_{III}^*} \int_0^{\frac{\rho_{III}^*}{t_p}} \tau_n \left(\frac{r}{t_p}\right) \mathrm{d}\left(\frac{r}{t_p}\right). \tag{4}$$

The effective notch stress parameter $S_{e,III} = \Delta\tau_e$ becomes in case of non-symmetry with respect to $(t_p/2)$:

$$\begin{aligned} S_{e,\mathrm{III}} = \frac{\Delta\tau_s}{\lambda_\tau}\frac{t_p}{\rho_\mathrm{III}^*} \Bigg\{ & \cos(\lambda_\tau\beta_a)\mu_{\tau F}\left(\frac{\rho_\mathrm{III}^*}{t_p}\right)^{\lambda_\tau} - \lambda_\tau\left(\frac{\rho_\mathrm{III}^*}{t_p}\right)\cdot \\ & \left[\left(\frac{\rho_\mathrm{III}^*}{t_p}\right)(\mu_{\tau M} + r_{\tau_s} + C_{tw}) - \mu_{\tau M} - C_{tw}\right] \Bigg\}. \end{aligned} \tag{5}$$

In case $\rho > 0$ and non-symmetry with respect to $(t_p/2)$ applies [20]:

$$\begin{aligned} S_{e,\mathrm{III}} = \frac{\Delta\tau_s}{\lambda_\tau}\left(\frac{t_p}{r_0+\rho_\mathrm{III}^*}\right) \Bigg\{ & \cos(\lambda_\tau\beta_a)\mu_{\tau F}\left[\left(\frac{r_0+\rho_\mathrm{III}^*}{t_p}\right)^{\lambda_\tau} - \left(\frac{r_0}{t_p}\right)^{\lambda_\tau}\right] - \\ & \left(\frac{r_0}{t_p}\right)^{2\lambda_\tau}\cos(\lambda_\tau\beta_a)\mu_{\tau F}\left[\left(\frac{r_0+\rho_\mathrm{III}^*}{t_p}\right)^{-\lambda_\tau} - \left(\frac{r_0}{t_p}\right)^{-\lambda_\tau}\right] - \\ & \lambda_\tau\frac{\rho_\mathrm{III}^*}{t_p}\left[\left(\frac{2r_0+\rho_\mathrm{III}^*}{t_p}\right)\left(\mu_{\tau M} + r_{\tau_s} + C_{tw}\right) - \mu_{\tau M} - C_{tw}\right] \Bigg\}. \end{aligned} \tag{6}$$

Mode-{I, III} formulations for symmetry with respect to $(t_p/2)$ have been developed as well, both for $\rho = 0$ and $\rho > 0$ (Appendix). The far field stress parameters $\{\Delta\sigma_s, r_{\sigma_s}; \Delta\tau_s, r_{\tau_s}\}$ can be obtained using nodal force output of relatively coarse meshed shell/plate FE models [70–72], naturally providing the constant membrane and linear bending contribution: $\sigma_s = \sigma_{sm} + \sigma_{sb}$, as well as the constant shear and linear torsion contribution: $\tau_s = \tau_{ss} + \tau_{st}$. The structural normal and shear stress ratios: $\{r_{\sigma_s} = \sigma_{sb}/\sigma_s, r_{\tau_s} = \tau_{st}/\tau_s\}$ reflect the far field stress gradients [8,20]. Eigenvalues $\{\lambda_{\sigma s}, \lambda_{\sigma a}, \lambda_\tau\}$, eigenvalue coefficients $\{\chi_{\sigma s}, \chi_{\sigma a}\}$ and stress angle β_a can be obtained using the notch angle α. Coefficients $\{\mu_{\sigma s}, \mu_{\sigma a}, \mu_{\tau F}, \mu_{\tau M}\}$ are obtained using force and moment equilibrium. The mode-I bending and mode-III torsion related weld load carrying stress coefficients, respectively C_{bw} and C_{tw}, are loading and geometry dependent. Fitting functions have been established [8,20]. A complete spatial description of a response cycle requires 2 parameters to be involved, important for modelling of sequence effects. The ranges $\{S_{e,I}, S_{e,III}\}$ and ratios $\{R_I = S_{e,I,min}/S_{e,I,max}, R_{III} = S_{e,III,min}/S_{e,III,max}\}$ are selected for this purpose. Adopting Walker's mean stress model, typically providing the best results for welded joints [7,20], the effective notch stress parameter becomes:

$$S_{e,eff} = \frac{S_e}{(1-R)^{1-\gamma}} \tag{7}$$

with $\{S_{e,eff} = S_{e,eff,I},\ S_e = S_{e,I},\ R = R_I,\ \gamma = \gamma_I\}$ for the mode-I and $\{S_{e,eff} = S_{e,eff,III},\ S_e = S_{e,III},\ R = R_{III},\ \gamma = \gamma_{III}\}$ for the mode-III effective notch stress component. The response ratio coefficient γ is a fitting parameter. For $\gamma \to 1$, the range dominates the fatigue resistance; the mean stress becomes governing for $\gamma \to 0$. However, an environment and service loading induced mean stress component is not the only one. Arc-welding adds a thermal loading induced – typically high-tensile – quasi-constant residual (mean) stress, affecting the fatigue strength. An explicit residual stress measure is typically not included, since for fatigue design in general only joints in as-welded (AW) condition are considered [e.g. 67,73,74], meaning any residual stress affecting the fatigue resistance is just implicitly incorporated in the most likely fatigue resistance parameter estimates. A stress relieving heat treatment can be applied, being one way to virtually eliminate residual stress and improve the fatigue strength. If both as-welded and stress-relieved (SR) test data are jointly considered, an explicit residual stress measure S_r has to be introduced to cover the thermal condition, meaning a re-formulation of the response ratio is required:

$$R_r = \frac{S_{e,min} + S_r}{S_{e,max} + S_r} = \frac{R\cdot S_e + S_r(1-R)}{S_e + S_r(1-R)}. \tag{8}$$

From fatigue design perspective, the as-welded condition is still adopted to define the reference resistance, meaning the stress-relieved data – principally without any residual stress – is expected to provide a compressive S_r estimate. Note that the extended R formulation most likely affect the mean stress sensitivity coefficient γ as well.

Because of the arc-welding induced heat input, the material crystallography changes, introducing a heat affected zone in between the weld and base material at the fatigue sensitive weld toe notch location. The hardness in the heat affected zone is typically large in comparison to the base material value. Since the weld material hardness is in general in between the heat affected zone and base material value,

an M-shaped hardness characteristic appears [75]. Applying a post-welding heat treatment is principally meant to reduce the hardness – in particular in the heat affected zone – and the aim is to obtain a more uniform hardness distribution across the material up to a certain extent, depending on parameters like heat rate, maximum temperature and treatment duration [75–77]. In general, an increased hardness reflects a smaller grain size and the other way around, introducing fatigue resistance consequences; i.e. changing crack initiation and growth behaviour. Since for a smaller grain size the initiation resistance seems to increase and at the same time the growth resistance decreases — for a larger grain size the opposite applies [78], dedicated material characteristic ρ^* parameters seem required for the as-welded and the stress-relieved condition.

Because of the mode-I and mode-III finite lifetime specific strength and mechanism fatigue resistance characteristics, a response level dependent shear strength coefficient $\beta(N)$ is adopted, rather than a constant one (Section 2.1). For a single-slope resistance relation $N = C \cdot S_e^m$:

$$\beta(N) = \frac{S_{e,I}(N)}{S_{e,III}(N)} = C_\beta \cdot N^{M_\beta} \tag{9}$$

with

$$C_\beta = 10^{\frac{\log(C_I)m_{III} - \log(C_{III})m_I}{m_I \cdot m_{III}}} \tag{10}$$

and

$$M_\beta = \frac{m_I - m_{III}}{m_I \cdot m_{III}}. \tag{11}$$

Since only the uniaxial mode-{I, III} number of cycles $\{N_I,\ N_{III}\}$ are known in advance, the actual $\beta(N)$ value has to be obtained in an iterative cycle counting process in order to capture N for the equivalent normal stress based von Mises type of criterion:

$$S_{e,eff} = \sqrt{\left\{ S^2_{e,eff,I} + \beta(N) \cdot S^2_{e,eff,III} \right\}}. \tag{12}$$

Counting iteratively the effective von Mises notch stress (Fig. 8) at the critical fracture plane (Section 2.2), the range $S_{e,i}$ including the normal and equivalent shear stress projections $\left\{S_{e,I,i}, \beta(N) \cdot S_{e,III,i}\right\}$ and corresponding ratios $\left\{R_I = S_{e,I,min,i}/S_{e,I,max,i}, R_{III} = \beta(N) \cdot S_{e,III,min,i}/[\beta(N) \cdot S_{e,III,max,i}]\right\}$ can be obtained for each cycle i (Section 2.3). Adopting a 0^{th}, 1^{st} or 2^{nd} order moment approach (Section 2.4), differences between the actual response path and the (straight) range have been used to incorporate a non-proportionality effect cycle-by-cycle in terms of C_{np}, including a material characteristic contribution in terms of c_m [34,35,49,50]:

$$S_{e,eff,i} = S_{e,i}\left(1 + c_m \cdot C_{np,i}\right) \tag{13}$$

with

$$C_{np,i} = \frac{\int_{\tilde{S}} (r \cdot |\sin(\theta)|)^n \mathrm{d}p}{\int_S (R \cdot |\sin(\theta)|)^n \mathrm{d}p} \quad \text{for } n = 0, 1 \text{ or } 2. \tag{14}$$

Although $C_{np,i}$ and c_m are meant to reflect respectively the path and material characteristic part, c_m may correct for any cycle counting and/or non-proportionality related model deficiency as well, since data fitting is used to obtain an estimate. A compromised value may be acquired, meaning interpretation becomes more difficult. In order to obtain a mid-cycle fatigue related equivalent effective notch stress parameter $S_{e,eq}$ for variable amplitude data fitting the constant amplitude data scatter band; i.e. $N(S_e) = C \cdot S_e^{-m}$ with $S_e = S_{e,eq}$, the linear damage model is adopted: $D = \sum\left\{n_i(S_{e,i})/N_i(S_{e,i})\right\} \leq 1$ with $N_i(S_{e,i}) = C \cdot S_{e,i}^{-m}$. For $D = 1$, reflecting failure, the formulation becomes:

$$S_{e,eq} = \left[\frac{\sum\{n_i(S_{e,i}) \cdot S^m_{e,i}\}}{N}\right]^{1/m}. \tag{15}$$

Recall $N = \sum\left\{n_i(S_{e,i})\right\}$, the iteratively obtained total number of effective von Mises notch stress cycles.

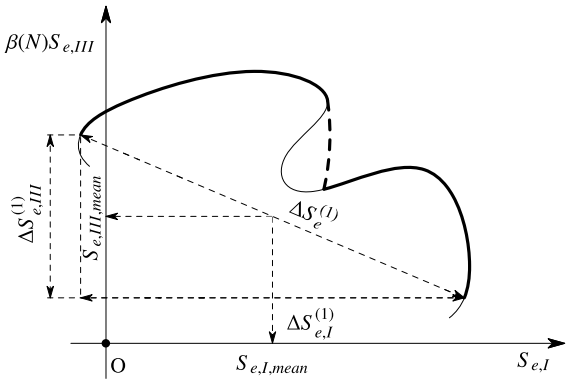

Fig. 8. Effective notch stress cycle characteristics in the von Mises plane.

3.2. Test data

Data series containing steel specimens with both tubular and planar structural joints have been considered (Fig. 9 and Tables 1 and 2), involving respectively circular/square hollow and plate cross-sections with specified joint dimensions (Fig. 7). Most data is obtained for constant amplitude loading conditions, but some variable amplitude data is included as well. Uniaxial mode-I, uniaxial mode-III and multiaxial mode-{I, III} response conditions – both proportional and non-proportional – have been introduced at the governing fatigue sensitive locations: SS welded butt joints and DS welded T-joints, as well as DS welded cruciform joints showing respectively non-symmetry and symmetry with respect to $(t_p/2)$ [8,20,61]. The governing hot spot is typically of the type C along the weld seam, although some of the type A at the weld end exist as well. Only specimens showing weld toe induced fatigue damage are included, involving predominantly failures and some run-outs. The data size is ~500.

The external loading consists of a normal force F_n or bending moment M_b for the mode-I response and a shear force F_s or torsion moment M_t for the mode-III response. Multiaxiality is often either loading [37,38,79–81,83–85,87,88,90] or geometry [86,89,91,92] induced. In case a mode-I and mode-III response related external loading component (e.g. M_b and M_t) are applied and at the same time the specimen contains a non-circular cross-section and warping constraints, multiaxiality includes even both a loading and geometry contribution [87,88]. The response is proportional by definition if multiaxiality is a result of geometry only. The response ratio $R = 0$ for the majority of the data series, reflecting a pulsating loading induced response condition with non-zero mean. For a significant amount of data $R = -1$, meaning the response condition is fully reversed and the mean component is zero. For the remaining data series, $R \neq \{0; -1\}$. Since data with both as-welded and stress-relieved thermal conditions are considered, the influence of (mean) residual stress has to be addressed as well. A von Mises based structural stress fatigue assessment (Fig. 10) of the adopted test data (Fig. 9 and Tables 1 and 2) shows the initial data scatter and the clear distinction between CA and (maximum range) VA results. Cycle counting is not involved for the multiaxial data and N is based on the mode-I lifetime.

3.3. Strength and mechanism contributions

The life time range of the considered data (Fig. 9 and Tables 1 and 2) virtually reflects mid-cycle fatigue characteristics only: $N = (10^4 \sim 5 \cdot 10^6)$ cycles. A log–log linear resistance formulation of the Basquin type typically relates N to a fatigue strength parameter S [7]: $\log(N) = \log(C) - m \cdot \log(S)$. Linear regression on life time is adopted to estimate the single-slope curve parameters: intercept $\log(C)$ and slope m, respectively reflecting a strength and mechanism contribution,

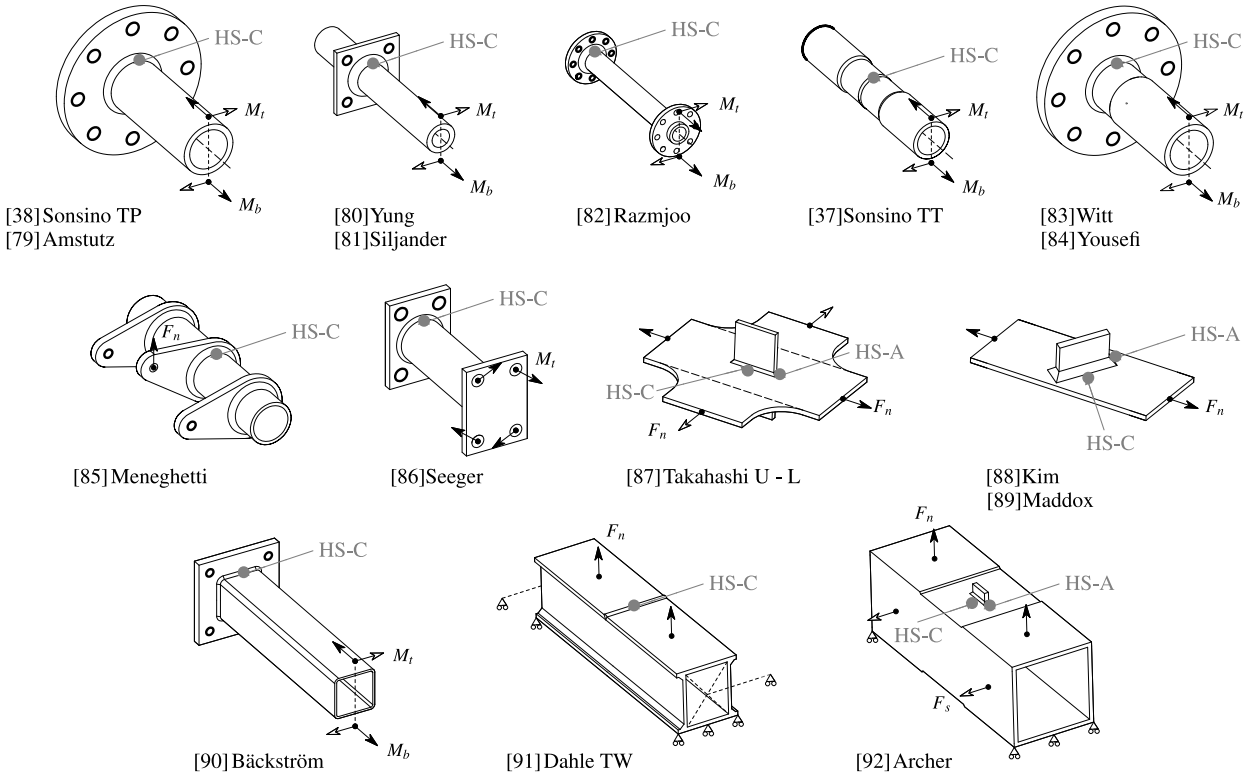

Fig. 9. Fatigue test specimen geometry, external loading (arrows) and constraints (thick lines or ⏃ symbols).

Table 1
Specimen characteristics of the fatigue resistance data from literature.

source	t_b [mm]	t_c [mm]	l_w [mm]	h_w [mm]	joint dimension [mm]	ρ [mm]	weld geometry	hot spot type	thermal condition
[38] Sonsino TP	10.0	25.0	9.0	9.0	⌀44.4 ∗ 10.0	0.45	SS T-joint	C	SR
[79] Yousefi	8.0	25.0	10.0	10.0	⌀42.4 ∗ 8.0	n.a.	SS T-joint	C	SR
[80] Siljander	9.5	9.5	8.0	8.0	⌀25.4 ∗ 9.5	0.18	SS T-joint	C	SR
[81] Witt	8.0	16.0	9.0	9.0	⌀44.4 ∗ 8.0	n.a.	SS T-joint	C	SR
[82] Seeger	8.0	20.0	6.3	6.3	⌀54.0 ∗ 8.0	1.00	SS T-joint	C	SR
[37] Sonsino TT	6.0	/	10.0	1.0	⌀44.4 ∗ 6.0	0.45	SS butt joint	C	SR
[83] Amstutz	7.7	25.0	9.0	9.0	⌀42.1 ∗ 7.7	1.00	SS T-joint	C	SR
[84] Razmjoo	3.2	12.0	11.0	11.0	⌀24.3 ∗ 3.2	0.18	SS T-joint	C	AW
[85] Yung	8.0	8.0	7.7	7.7	⌀23.8 ∗ 8.0	n.a.	SS T-joint	C	{SR, AW}
[86] Meneghetti	8.0	20.0	12.0	12.0	⌀50.8 ∗ 8.0	2.00	SS T-joint	C	{SR, AW}
[87] Bäckström	5.0	20.0	6.0	6.0	□100 ∗ 100 ∗ 5.0	1.00	SS T-joint	C	AW
[88] Archer	6.0	10.0	9.0	9.0	□200 ∗ 200 ∗ 6.0	n.a.	SS T-joint	{A, C}	AW
[89] Dahle TW	10.0	/	12.0	2.0	□150 ∗ 150 ∗ 10.0	n.a.	SS butt joint	C	AW
[90] Takahashi	12.0	12.0	6.0	6.0	▬1000 ∗ 1000 ∗ 12.0	n.a.	DS Cruciform joint	{A, C}	AW
[91] Maddox	12.5	12.5	9.0	9.0	▬ 700 ∗ 160 ∗ 12.5	n.a.	SS T-joint	{A, C}	AW
[92] Kim	9.0	9.0	9.0	9.0	▬1000 ∗ 200 ∗ 9.0	n.a.	SS T-joint	{A, C}	AW

introducing the life time scatter (i.e. performance) parameter σ_N. For strength performance evaluation purposes, the scatter band index $T_{\sigma S} = 1 : (S_{10}/S_{90})$ will be used: the fatigue strength ratio for 10 [%] and 90 [%] probability of survival [69]. Maximum likelihood based regression [61,93] will be employed to obtain the most likely parameter vector estimate $\boldsymbol{\Phi} : \max\{\mathcal{L}(\boldsymbol{\Phi}; N|S); \boldsymbol{\Phi}\}$ with $\boldsymbol{\Phi} = \{\log(C), m, \sigma_N\}$, assuming fatigue lifetime N is most likely log(Normal) distributed [8,20]. For $S = S_{e,eff}$ (Section 3.1), the response ratio coefficient and material characteristic length providing respectively another strength and mechanism contribution are introduced, principally extending the parameter vector to: $\boldsymbol{\Phi} = \{\log(C), \gamma, m, \rho^*, \sigma_N\}$. Note that ideally the uniaxial mode-I and mode-III, as well as the multiaxial proportional and non-proportional mode-{I, III} data (Fig. 9 and Tables 1 and 2) would have been balanced for appropriate S_e performance evaluation, meaning that except the σ_N and $T_{\sigma S}$ parameters as global indicators for all data, the individual data groups behaviour have to be carefully considered as well.

Starting with the uniaxial reference fatigue resistance in terms of S_e, the mode specific strength and mechanism coefficients will be established first (Section 3.3.1) in order to obtain $\beta(N)$. The S_e performance for multiaxial fatigue resistance data will be investigated accordingly (Section 3.3.2). Particular attention will be paid to the consequences of mode specific strength and mechanism for mixed mode-{I, III} fatigue and the influence of non-proportionality. Since S_e is an equivalent normal stress von Mises type of parameter, the fitting of the multiaxial data in the mode-I uniaxial data scatter band will be verified, as well as the fitting of VA data in the CA data scatter band in order to establish the performance of the adopted linear damage accumulation model for a $S_{e,eff}$ based fatigue assessment.

3.3.1. Uniaxial reference fatigue resistance

The S_e based mode-I mid-cycle fatigue resistance formulation for planar structures in steel (maritime) structures, involving hot spot types {A, B, C} and various as-welded joint geometries, has already been

Table 2
Loading characteristics of the fatigue resistance data from literature.

source	uniaxial mode-I		uniaxial mode-III		multiaxial mode-{I, III}			loading	no. specimens		
	R_{I}	loading	R_{III}	loading	R_{I}	R_{III}	loading	condition	I	III	{I, III}
[38] Sonsino TP	-1	M_b	-1	M_t	-1	-1	$M_b + M_t$	{CA, VA}	21;	9;	29
[79] Yousefi	$[0;-1]$	M_b	-1	M_t	$[0;-1]$	$[0;-1]$	$M_b + M_t$	{CA, VA}	38;	14;	82
[80] Siljander	$[0;-1]$	M_b	$[0;-1]$	M_t	$[0;-1]$	$[0;-1]$	$M_b + M_t$	CA	10;	8;	20
[81] Witt	-1	M_b	-1	M_t	$[0;-1]$	$[0;-1]$	$M_b + M_t$	CA	11;	11;	19
[82] Seeger	/	/	-1	M_t	/	/	/	CA	0;	6;	0
[37] Sonsino TT	-1	M_b	/	/	-1	-1	$M_b + M_t$	CA	14;	0;	24
[83] Amstutz	$[0;-1]$	M_b	-1	M_t	$[0;-1]$	$[0;-1]$	$M_b + M_t$	CA	12;	7;	19
[84] Razmjoo	0	F_n	0	M_t	0	0	$F_n + M_t$	CA	7;	8;	13
[85] Yung	-1	M_b	-1	M_t	-1	-1	$M_b + M_t$	CA	5;	2;	7
[86] Meneghetti	/	/	/	/	0.1	0.1	F_n	CA	0;	0;	14
[87] Bäckström	[0.1 ... 0.7]	M_b	-1	M_t	[0.4 ... 1.1]	[−1.3 ... 0]	$M_b + M_t$	CA	5;	4;	13
[88] Archer	0	M_b	-1	F_s	0	-1	$M_b + F_s$	CA	1;	12;	18
[89] Dahle TW	-1	M_b	/	/	-1	-1	M_b	CA	3;	0;	5
[90] Takahashi	0	F_n	/	/	0	0	$F_n + F_n$	CA	6;	0;	11
[91] Maddox	0	F_n	/	/	0	0	F_n	CA	6;	0;	12
[92] Kim	0	F_n	/	/	0	0	F_n	CA	13;	0;	27

established for CA data [94] and shows an excellent performance as reflected in the lifetime standard deviation: $\sigma_N = 0.21$. The intercept and slope values are: $\log(C_I) \sim 13.28$ and slope $m_I \sim 3.12$. Note that the slope is close to the typical design value $m = 3$ [67,73]. Assuming $\rho = 0$, a most likely $\rho_I^* \sim 1.34$ has been obtained, suggesting the major part of the fatigue lifetime is spent in the notch affected region indeed. The response ratio coefficient $\gamma_{I,AW} \sim 0.90$ implies a predominant contribution of stress range over mean stress as a consequence of the typically high-tensile welding induced residual stress. Since the data size of the considered (predominant) tubular and (some) planar mode-I data (Tables 1 and 2) is ~140, relatively small in comparison to the ~2500 assessed before [94], enforcing $\log(C_I) \sim 13.28$, $m_I \sim 3.12$, $\rho_I^* \sim 1.34$ and $\gamma_{I,AW} \sim 0.90$ seems straightforward from parameter confidence perspective. For the stress-relieved joints, $\gamma_{I,AW} \sim 0.90$ is initially still adopted in case $R \geq 0$, although expected to be too large because of eliminated residual stress. Assuming only the tensile part of the cycle contributes to fatigue damage accumulation, $\gamma_{I,SR} = 0$ has been used for $R < 0$, based on a crack opening mode-I requirement [7]. The parameter vector becomes: $\boldsymbol{\Phi} = \{\sigma_N\}$.

Regression analysis of all data shows that intercept $\log(C)$ and slope m, hardly changed in comparison to the reference data values [94], since the amount of added data (Fig. 9 and Tables 1 and 2) is relatively small. The AW data fits the reference data scatter band reasonably well

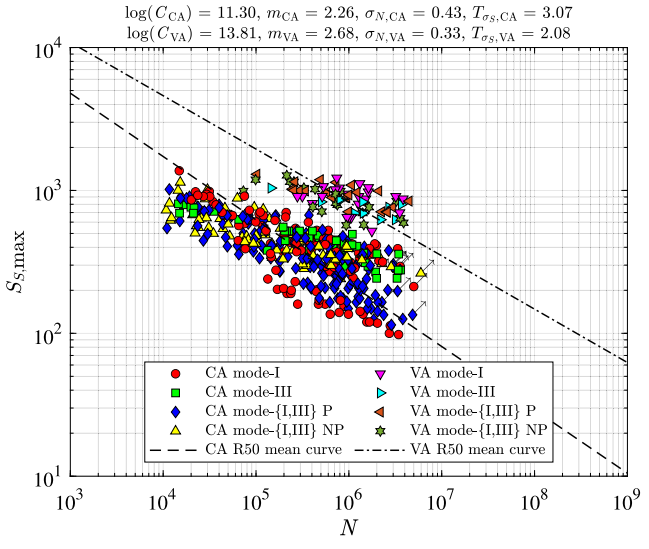

Fig. 10. Structural stress based fatigue resistance.

(Fig. 11). However, the fatigue strength and mechanism of SR data seems different, as reflected in the scatter and non-fitting behaviour, explaining the increased σ_N. Introducing for the SR data a residual stress S_r and response ratio coefficient $\gamma_{I,SR}$, covering the full R range like for AW data (Section 3.1), extends the parameter vector to: $\boldsymbol{\Phi} = \{\log(C_I), S_r, \gamma_{I,SR}, m_I, \sigma_N\}$. The SR data fit in the reference AW data scatter band improved indeed with respect to strength and mechanism: $\log(C)$ and m (Fig. 12). The most likely residual stress S_r proved to be compressive (Section 3.1), confirming the (average) residual stress for the AW data is highly tensile indeed. Mean residual stress coefficient $\gamma_{I,SR} \sim 0.6$ reflects an almost balanced contribution from stress range and mean residual stress, like for $\gamma = 0.5$ [7]. Since $\gamma_{I,SR} \neq 0$ in case $R < 0$ for the SR joints and $\gamma_{I,SR}$ applies for the full R range, suggests some residual stress is still present. However, the residual stress consists of an equilibrium equivalent and self-equilibrium part as well [61]. A stress-relieving heat treatment could very well eliminate the equilibrium equivalent part, but the self-equilibrium part – highly tensile in the notch affected region, – may still exist. The lifetime standard deviation σ_N has reduced, but is still larger than the original reference data value as the data scatter indicates, suggesting another modelling step is required. Because of the differences in material crystallography for AW and SR data (Section 3.1), a dedicated material characteristic strength parameter can be introduced, meaning: $\boldsymbol{\Phi} = \{\log(C_I), S_r, \gamma_{I,SR}, m_I, \rho^*_{I,SR}, \sigma_N\}$. The $\rho^*_{I,SR} \sim 3.86$ estimate turns out to be larger than the AW value: $\rho^*_{I,AW} \sim 1.34$ (Fig. 13). Since a stress relieving heat treatment in general decreases the hardness, the initiation resistance decreases and the growth resistance increases (Section 3.1), suggesting a decreased fatigue resistance. However, the positive effect of eliminated residual mean stress consequences exceeds the negative influence of the ρ^* decrease, still providing an increased fatigue resistance when a stress relieving heat treatment is applied. The most likely residual stress estimate S_r changed somewhat, but surprisingly the residual mean stress coefficient $\gamma_{I,SR}$ has become about equal to the AW value $\gamma_{I,AW}$, meaning the stress range contribution dominates anyway. Yet, the most important result seems the reduced lifetime data scatter σ_N, principally the same value as obtained for just the reference data. At the same time, $\sigma_N \sim 0.27$ for the considered data (Fig. 9 and Tables 1 and 2) only; at least a matter of data size as reflected in the parameter confidence (Table 3). The corresponding strength scatter band index $T_{\sigma S_e} = 1 : 1.67$ and turns out to be larger than a typical value of $1 : 1.50$ [10]. At first glance, the VA data fits the CA data scatter band for $D = 1$, supporting the hypothesis that advanced fatigue damage criteria – including the mean stress as an important sequence parameter in terms of R and γ – contributes to the (linear) damage accumulation model performance (Section 2.5).

The S_e based mode-III mid-cycle fatigue resistance parameter estimates and confidence (Fig. 14,Table 3) for tubular structures in steel

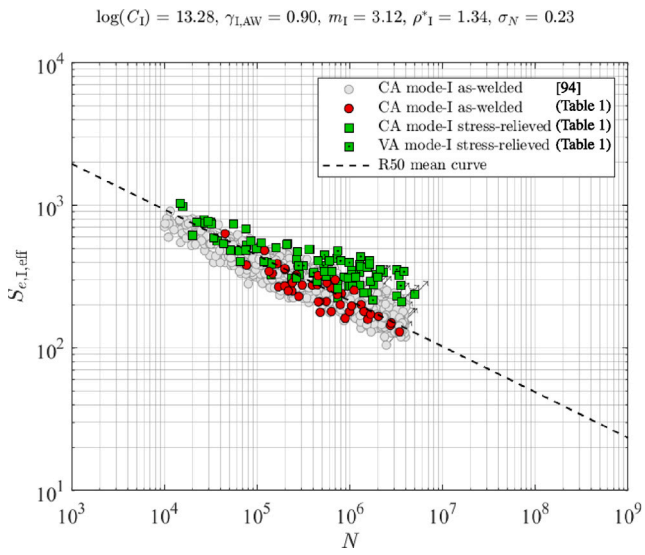

Fig. 11. Mode-I data effective notch stress based fatigue resistance, including mean stress correction.

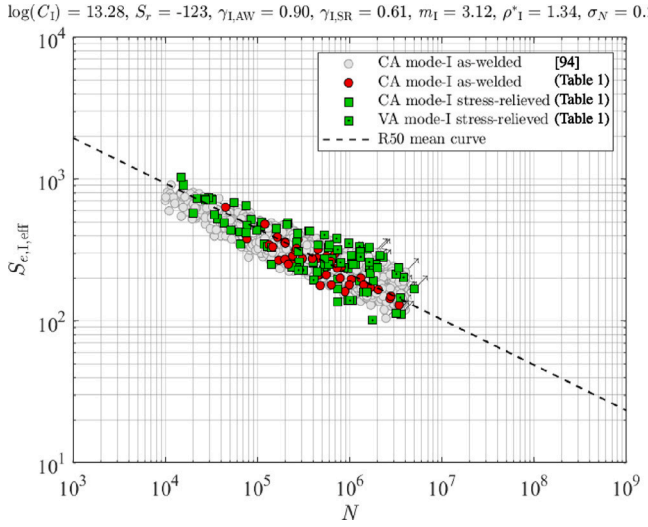

Fig. 12. Mode-I data effective notch stress based fatigue resistance, including mean and residual stress correction.

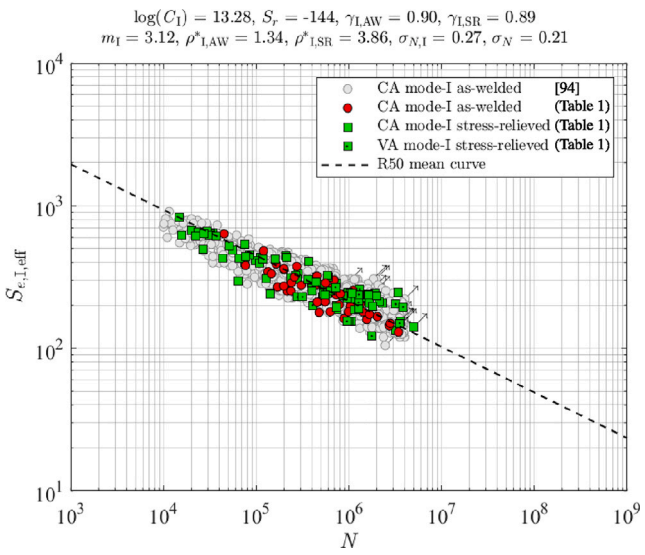

Fig. 13. Mode-I data effective notch stress based fatigue resistance, including mean and residual stress correction with dedicated $\rho^*_{I,AW}$ and $\rho^*_{I,SR}$.

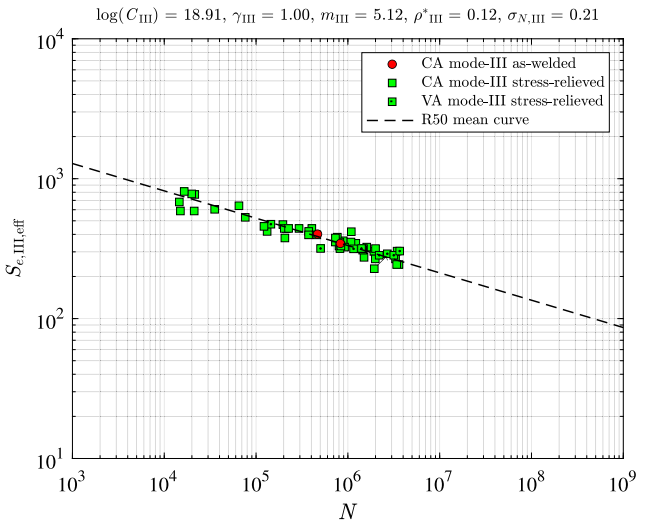

Fig. 14. Mode-III data effective notch stress based fatigue resistance, including mean stress correction.

(maritime) structures, principally involving hot spots type C and a DS welded T-joint geometry only (Fig. 9 and Tables 1 and 2), have already been established for CA data [20]. The data size is ~50. Excellent performance has been obtained, as reflected in the lifetime standard deviation: $\sigma_{N,III} \sim 0.21$; basically the same value as obtained for the mode-I reference data, but way smaller than the value for the considered data: $\sigma_{N,I} \sim 0.27$. The difference in lifetime scatter between mode-I and mode-III could partially be related to the type of loading and the geometry, reflecting a volume (i.e. weld seam length) effect. For the mode-I data on the one hand, most specimens are subjected to a bending moment M_b and have a tubular, circular hollow cross-section (Fig. 9). The governing hot spot and most likely fatigue failure position is observed at one location along the weld seam, principally independent of the fabrication aspects induced weakest link; a matter of production tolerances and welding induced defects. On the other hand, for the mode-III data a torsion moment M_t is typically applied and for tubular, circular hollow cross-sections all locations along the weld seam are identified as hot spot. Fatigue failure develops at the position of the fabrication defined weakest link, like the location of the welding induced extreme defect. The mode-III fatigue strength scatter band index $T_{\sigma S_e} = 1 : 1.27$ is smaller than a typical value of 1 : 1.50 [10]. Intercept $\log(C_{III}) \sim 18.91$ and slope $m_{III} \sim 5.12$ have been obtained as most likely values. Note that the slope is close to the typical design

Table 3
Effective notch stress based parameter estimates and 75[%] lower and upper confidence bounds for mode-I and mode-III.

parameter	mode-I		mode-III	
$\log(C)$	13.28	[13.20, 13.36]	18.91	[18.17, 19.64]
m	3.12	[3.08, 3.15]	5.12	[4.85, 5.37]
ρ^*	/	/	0.12	[0.07, 0.21]
ρ^*_{AW}	1.34	[1.22, 1.45]	/	/
ρ^*_{SR}	3.85	[3.56 4.16]	/	/
γ	/	/	1.00	[0.98, 1.00]
γ_{AW}	0.90	[0.88, 0.91]	/	/
γ_{SR}	0.89	[0.87, 0.91]	/	/
S_r	−144	[−144, −143]	/	/
σ_N	0.27	[0.25, 0.29]	0.21	[0.18, 0.24]
σ_N incl. [94]	0.21	[0.19, 0.23]	/	/

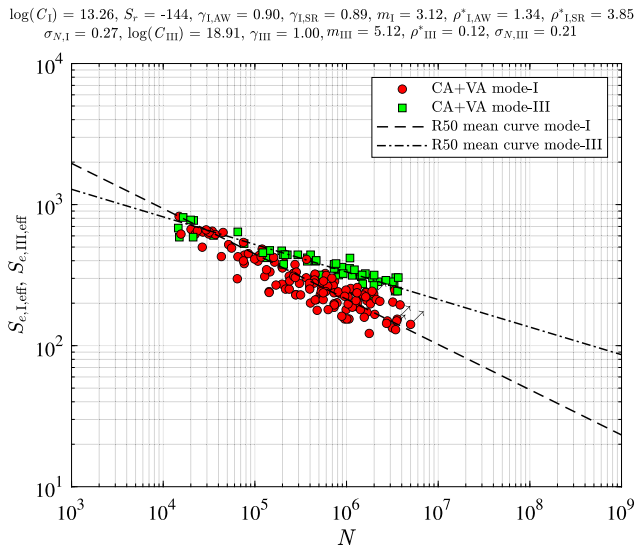

Fig. 15. Uniaxial mode-I and mode-III data effective notch stress based fatigue resistance.

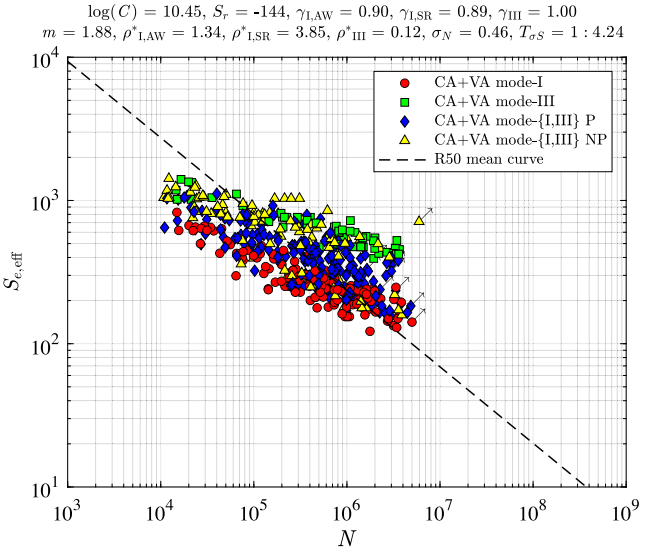

Fig. 16. Effective notch stress based fatigue resistance for uniaxial and multiaxial data; $\rho^*_{\mathrm{I}} \neq \rho^*_{\mathrm{III}}$ and $\beta = \sqrt{3}$.

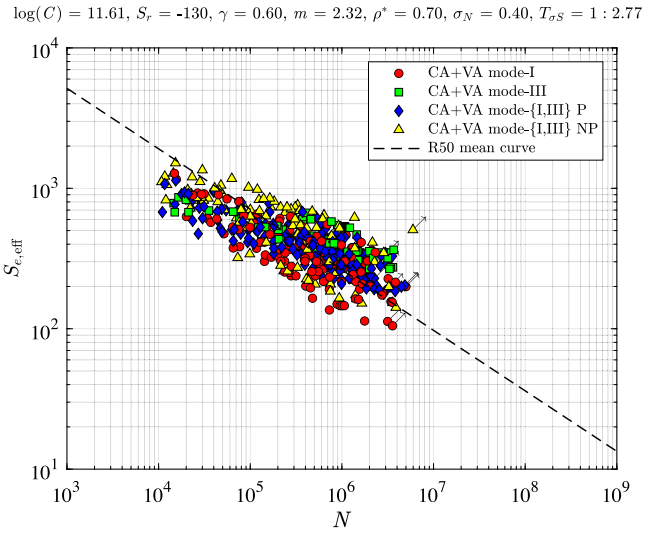

Fig. 17. Effective notch stress based fatigue resistance for uniaxial and multiaxial data; $\rho^*_{\mathrm{I}} = \rho^*_{\mathrm{III}}$ and $\beta = \sqrt{3}$.

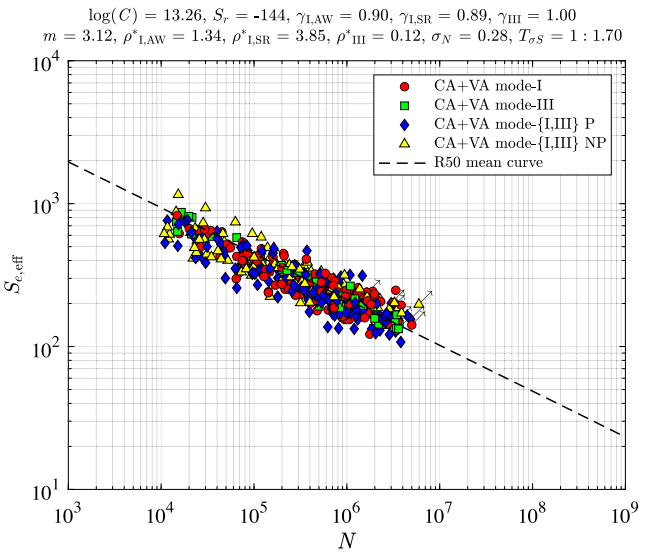

Fig. 18. Effective notch stress based fatigue resistance for uniaxial and multiaxial data; $\rho^*_{\mathrm{I}} \neq \rho^*_{\mathrm{III}}$ and $\beta = f(N)$.

value $m = 5$ [67,73]. The real weld notch radius has been required to be included in order to obtain $\rho^*_{III} \sim 0.12$. Since $m_{III} > m_I$ and $\rho^*_{III} < \rho^*_I$, the mode-III damage process seems in comparison to mode-I even more an initiation related near-(notch) surface phenomenon [20]. The response ratio coefficient $\gamma_{III} \sim 1$, meaning (residual) stress hardly affects the mode-III fatigue resistance and distinguishing different thermal conditions seems not relevant (Fig. 14). Like for the uniaxial mode-I assessment, the linear damage accumulation up to $D = 1$ shows VA data fitting the CA data scatter band.

A comparison of mode-I and -III data and mean (i.e. 50 [%] reliability) $S_e - N$ curves clearly shows differences in both strength and mechanism (Fig. 15), i.e. in $\{\log(C), \gamma\}$ and $\{m, \rho^*\}$, implying a lifetime dependent shear strength coefficient $\beta(N)$ rather than a constant one is required for multiaxial fatigue assessment (Section 3.1).

3.3.2. Multiaxial fatigue resistance

Involving the multiaxial fatigue data (Fig. 9 and Tables 1 and 2), the normal stress equivalent von Mises type of failure criterion is adopted (Eq. 12): $S_e = \sqrt{\left[S_{e,I,eff}(\gamma_I, \rho^*_I)^2 + \beta(N) \cdot S_{e,III,eff}(\gamma_{III}, \rho^*_{III})^2\right]}$. Note that for the single sided (SS) welded butt joints the $S_{e,III}$ related C_{tw} estimate (Eq. 6) is obtained using the formulation as principally established for DS welded T-joints, assuming $t_c = 0$ [20]. For CA mixed mode-{I, III} data involving asynchronous behaviour and/or different frequencies, as well as for VA multiaxial data, cycle counting in the von Mises plane is initially adopted without any material characteristic non-proportionality effects: $c_m = C_{np} = 0$ (Eq. 13). In order to illustrate the importance of strength and mechanism contributions, reflected in the $\beta(N)$ related $\{\log(C), m\}$ and the S_e based mode-I and material crystallography dependent $\{\gamma, \rho^*\}$ parameters, regression analysis results for $\beta = \sqrt{3}$ as well as for $\gamma_I = \gamma_{III}$ and $\rho^*_I = \rho^*_{III}$ are provided for reference purposes (Figs. 16 and 17). The parameter vectors have been $\boldsymbol{\Phi} = \left\{\log(C), S_r, \gamma_{I,AW}, \gamma_{I,SR}, \gamma_{III}, m, \rho^*_{I,AW}, \rho^*_{I,SR}, \rho^*_{III}, \sigma_N\right\}$ and $\boldsymbol{\Phi} = \left\{\log(C), S_r, \gamma, m, \rho^*, \sigma_N\right\}$ respectively.

In comparison to the structural stress based results (Fig. 10), it is clear that adopting the effective notch stress as strength criterion

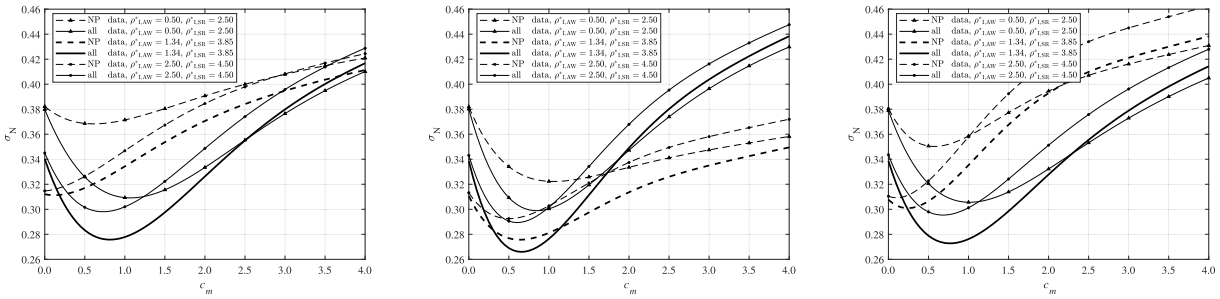

Fig. 19. Most likely σ_N for a range of c_m in case of three different ρ_I^* values and $\rho_{III}^* = 0.12$. Path dependent non-proportionality: 0th moment (left), 1st moment (centre) and 2nd moment (right).

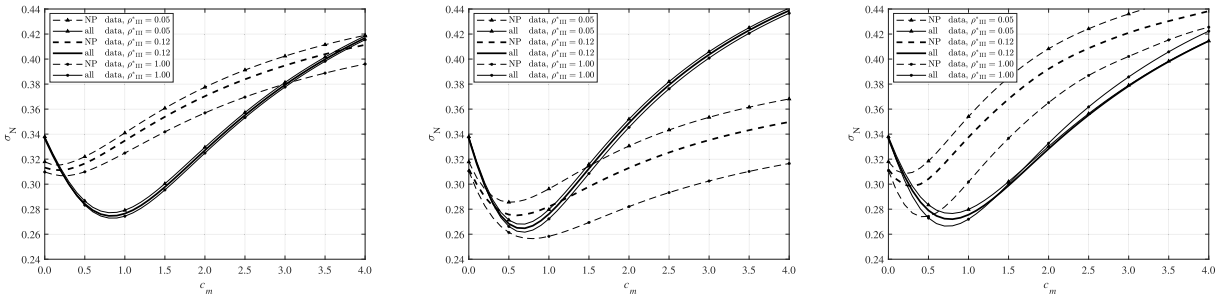

Fig. 20. Most likely σ_N for a range of c_m in case of three different ρ_{III}^* values and $\rho_{I,AW}^* = 1.34$ and $\rho_{I,SR}^* = 3.85$. Path dependent non-proportionality: 0th moment (left), 1st moment (centre) and 2nd moment (right).

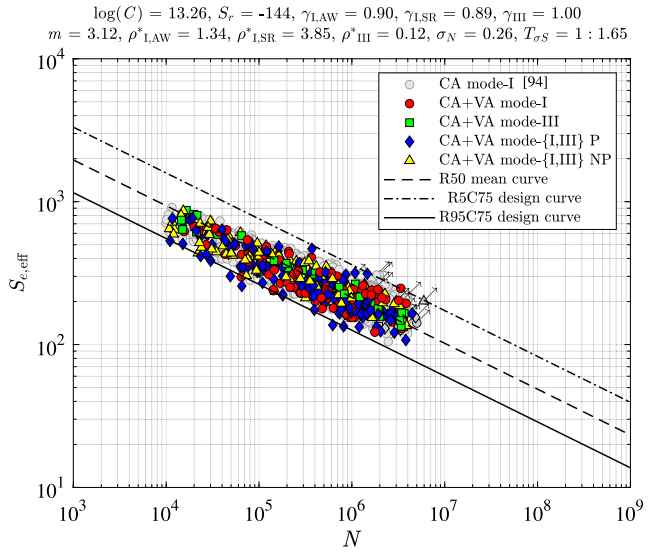

Fig. 21. Effective notch stress based fatigue resistance for uniaxial and multiaxial data; $\rho_I^* \neq \rho_{III}^*$, $\beta(N)$, 1st order path dependent non-proportionality with $c_m = 0.65$.

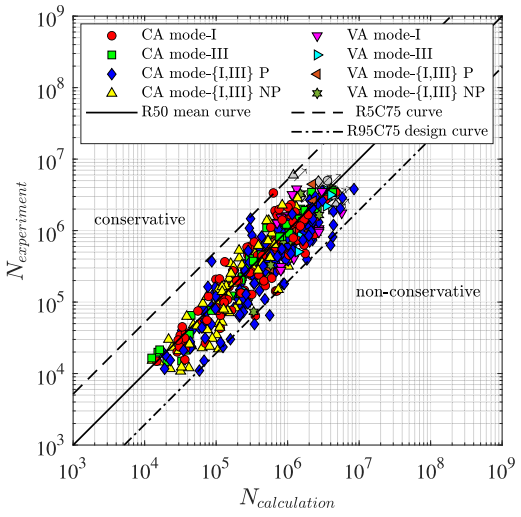

Fig. 22. Lifetime ratio plot of effective notch stress based fatigue resistance for uniaxial and multiaxial data; $\rho_I^* \neq \rho_{III}^*$, $\beta(N)$, 1st order path dependent non-proportionality with $c_m = 0.65$.

and cycle counting allows to enclose in the same scatter band CA and VA data. At the same time, the overall lifetime standard deviation is significantly reduced.

The different strength and mechanism for the uniaxial mode-I and mode-III as well as the multiaxial mode-{I, III} P and NP data can clearly be observed in the separate data scatter bands for $\beta = \sqrt{3}$, reflected in the imaginary intercept and slope for each data group (Fig. 16). The lifetime scatter parameter $\sigma_N \sim 0.46$ and corresponding strength index $T_{\sigma S_e} = 1 : 4.24$ illustrate in comparison to the uniaxial values: $\sigma_{N,I} \sim 0.27$, $\sigma_{N,III} \sim 0.21$, $T_{\sigma S_e,I} = 1 : 1.67$ and $T_{\sigma S_e,III} = 1 : 1.27$ (Section 3.3.1) a much worse fit. Eliminating in addition the S_e related mode and material sensitive strength and mechanism contributions changes the imaginary intercept and slope for each data group (Fig. 17), but improves the overall performance: $\sigma_N \sim 0.40$ and $T_{\sigma S_e} = 1 : 2.77$. However, the data scatter of the individual data groups even increased, suggesting the equivalent shear strength and effective notch stress based strength and mechanism contributions are important. Overall, the uniaxial mode-I and multiaxial mode-{I, III} P data shows a reasonable fit, but the uniaxial mode-III and mode-{I, III} NP data are way out of range (Figs. 16 and 17), illustrating at the same time the consequences of data imbalance (Section 3.2). Without affecting the global performance lifetime and strength parameters σ_N and $T_{\sigma S_e}$, the relative position of groups of data can change significantly and may cause wrong conclusions regarding the importance of strength

Table 4
Lifetime standard deviation σ_N and strength scatter band index $T_{\sigma S}$ for different multiaxial fatigue assessment concepts.

source	developer	failure criterion	damage plane	cycle counting	non-proportionality measure	damage accumulation	σ_N	$T_{\sigma S}$
Eq. (12)	Bufalari et al.	[a] non-linear eq. stress: von Mises type with $\beta(N)$	critical	multiaxial: von Mises plane	path: 1st order (cycle-by-cycle)	linear	0.26	1:1.65
[21]	IIW (guidelines)	[b] non-linear eq. stress: von Mises type with $\beta(S\|N = 2 \cdot 10^6)$	critical	uniaxial	damage down grade	linear	0.46	1:2.69
[95]	IIW (guidelines)	[b] non-linear eq. stress: von Mises type with $\beta(S\|N = 2 \cdot 10^6)$	critical	uniaxial	damage down grade	linear	0.42	1:2.28
[21]	CEN (Eurocode)	[b] non-linear eq. stress: damage mode superposition based	critical	uniaxial	/	linear	0.40	1:2.65
[95]	CEN (Eurocode)	[b] non-linear eq. stress: damage mode superposition based	critical	uniaxial	/	linear	0.49	1:2.62
[21]	/	[b] max principal stress	critical	uniaxial	/	linear	0.51	1:3.45
[21]	/	[b] von Mises stress with $\beta = \sqrt{3}$	critical	uniaxial	/	linear	0.44	1:2.41
[21]	Sonsino	[b] non-linear eq. stress: von Mises type with $\beta(S)$	integral	uniaxial	in failure criterion (cycle-by-cycle)	linear	0.58	1:6.04
[21]	Carpinteri et al.	[b] non-linear eq. stress: von Mises type with $\beta(N)$	critical	multiaxial: main+aux. channel	in failure criterion (cycle-by-cycle)	non-linear	0.47	1:2.81
[21]	Findley	[b] linear eq. stress	critical	uniaxial	/	linear	0.46	1:2.40
[21]	Susmel	[b] shear stress	invariant	uniaxial	in resistance curve (time series VAR)	linear	0.48	/
[95]	Dong et al.	[c] non-linear eq. stress: von Mises type with $\beta = \sqrt{3}$	critical	multiaxial: von Mises plane	path: 1st order (cycle-by-cycle)	linear	0.36	1:2.03

Fatigue strength parameter:
[a] effective notch stress using material characteristic length
[b] effective notch stress using fictitious notch radius
[c] traction equivalent structural stress

and mechanism contributions as observed before [34,35,95]. Adopting the mode specific and material characteristic strength and mechanism contributions; $\{\log(C), m\}$ in terms of $\beta(N)$ – for an iteratively obtained N value (Section 3.1) – and $\{\gamma, \rho^*\}$, significantly improves the model performance (Fig. 18). The lifetime scatter and strength scatter band index reduced to a value about equal to that of the uniaxial mode-I data: $\sigma_N \sim 0.28$ (Section 3.3.1) and $T_{\sigma S_e} = 1 : 1.70$. However, the multiaxial NP data group still shows room for improvement.

Adopting a 0th, 1st or 2nd order moment approach (Section 3.1), differences between the actual response path and the (straight) range have been used to incorporate non-proportionality cycle-by-cycle in terms of C_{np} (Eq. 14), including a material characteristic contribution c_m (Eq. 13). The $c_m - \sigma_N$ sensitivity has been investigated for the C_{np} defined 0th, 1st and 2nd order moment approaches to evaluate the model performance. At the same time, the influence of ρ^* has been explored up to some extent, running the sensitivity analysis for the most likely mode-I and mode-III ρ^* estimate, as well as a smaller and larger value (Figs. 19 and 20). Since data is unbalanced, i.e. the multiaxial NP data size is relatively small, the performance for the multiaxial NP data only as well as all data has been considered. Looking at the $c_m - \sigma_N$ sensitivity for varying ρ^*_{III} (Fig. 20), the trendlines do not change much. However, in contrast to the results for varying ρ^*_I, the sensitivity is approximately ρ^*_{III} independent considering all data, since the governing scatter contribution is mode-I related (Figs. 12 and 13). An optimum c_m still exists for the 0th, 1st and 2nd order approach. Again, the best performance is obtained for a 1st order approach and a coinciding optimum for both the multiaxial NP data only and all data is observed. However, for a smaller ρ^*_{III} an even better performance – still for $c_m \sim 0.65$ – is obtained, basically confirming that c_m corrects in addition for any cycle counting and/or non-proportionality related model deficiency indeed. Assessing all data (Fig. 9 and Tables 1 and 2) using the most likely mode and material specific strength contributions, $\{\log(C), m\}$ and $\{\gamma, \rho^*\}$ respectively represented in $\beta(N)$ and S_e, as well as the 1st order approach to obtain C_{np} cycle by cycle for $c_m \sim 0.65$ in case of non-proportionality, an even better performance is obtained. The lifetime scatter has reduced to $\sigma_N \sim 0.26$ and the strength scatter band to $T_{\sigma S_e} = 1 : 1.65$. (Figs. 18 and 21). Principally all data fits the mode-I reference data scatter band, i.e. the interval in between 5 and 95 [%] reliability for 75 [%] confidence (Figs. 21 and 22). Note that an increased data size: currently ~500 for the assessed data (Fig. 9 and Tables 1 and 2) and ~2500 for the mode-I reference data, can contribute to another σ_N reduction.

The multiaxial mode-{I, III} P data appears to show the largest scatter. However, the uniaxial mode-I and mode-III resistance (material) characteristics have been explicitly incorporated, as well as multiaxial mode-{I, III} non-proportionality measures, meaning that only for the multiaxia mode-{I, III} P data no specific resistance aspects have been considered; an obvious requirement to continue the improvement of the fatigue resistance formulation. Aside from improved damage plane selections, cycle counting algorithms and/or non-proportionality measures, failure criterion aspects could be reconsidered as well. One possible research direction could be to incorporate a shear strength coefficient based on times series rather than a peak–valley sequence analysis, i.e. instantaneous rather than cycle-by-cycle; $\beta(t)$ rather than $\beta(N)$, implying even the multiaxial P data would show NP behaviour in the von Mises stress plane. However, a redefinition of the failure criterion may be required as well, since the S_e formulation is currently based on a cycle characteristic parameter: the (effective) stress range. Another direction might be the introduction of coupling terms, for example like $S_e = \sqrt{C_1 \cdot S^2_{e,I} + C_2 \cdot S_{e,I} \cdot S_{e,III} + C_3 \cdot S^2_{e,III}}$. To illustrate: mean (residual) stress effects for uniaxial mode-III fatigue might be negligible, but may be relevant if a mode-I contribution is involved as well [e.g. 96]. Mode and material specific uniaxial $\{\log(C), \gamma, m, \rho^*\}$ parameters have been established to assess multiaxial data, but missing mode-{I, III} interaction could explain the multiaxial proportional data scatter. The variable amplitude data fits the constant amplitude data

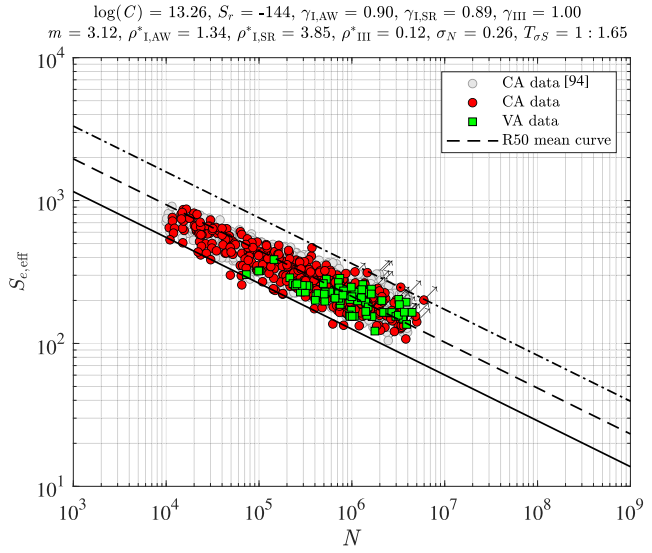

Fig. 23. Effective notch stress based fatigue resistance for uniaxial and multiaxial, constant and variable amplitude data.

scatter band for $D = 1$ (Fig. 23), supporting the hypothesis that an advanced fatigue failure criterion like S_e contributes to the (linear) damage accumulation model performance. However, most variable amplitude data involves a random sequence reflected in a Normal distributed narrow-band spectrum (Fig. 24), meaning the data contains at maximum an averaged sequence effect. A response based non-linear damage model (Section 2.5) may still be required if data for different types of random sequence (e.g. broad-band spectra) or even for a determined sequence will be incorporated.

In comparison to the assessment for other combinations of failure criterion, damage plane, cycle counting algorithm, non-proportionality measure and damage accumulation model in terms of lifetime and strength scatter; i.e. σ_N and $T_{\sigma S_e}$, the outperformance is impressive (Table 4). In principle only the effective notch stress is considered for the sake of fair judgement, although one mode and material invariant fictitious notch radius is adopted to obtain an S_e estimate at once, rather than averaging the stress distribution over a material characteristic length to obtain the actual S_e [43,66–69,97,98]. One exception is the equivalent traction based structural stress; a cracked rather than intact geometry based parameter, considered because a similar cycle counting algorithm is involved.

Results from other sources (Table 4) do not consider all the data available (Fig. 9 and Tables 1 and 2), meaning in general a better fit than when all data is involved and emphasizing at the same time the quality of the obtained performance criteria: $\sigma_N \sim 0.26$ and $T_{\sigma S_e} = 1 : 1.65$. Using not the same data sets partially explains the differences for the multiple IIW and Eurocode results as well. Note that the lifetime scatter parameter σ_N is not proportional to the corresponding strength scatter band index (Table 4), since $T_{\sigma S_e}$ is slope dependent: $T_{\sigma S} = 1 : (S_{e,10}/S_{e,90})$ with $S_{e,p_s} = \left\{N \cdot \left(C \cdot 10^{\Phi^{-1}(1-p_s)\cdot\sigma_N}\right)^{-1}\right\}^{-1/m}$ and $\Phi^{-1}(1-p_s)$ the inverse of the adopted Normal distributed probability density function for probability of survival p_s, meaning $(S_{e,10}/S_{e,90}) = \left\{10^{\sigma_N\left(\Phi^{-1}(1-0.10)-\Phi^{-1}(1-0.90)\right)}\right\}^{1/m}$. Anyway, both the lifetime scatter and strength scatter band index are not yet similar to the reference mode-I data values [94]: $\sigma_N = 0.21$ and $T_{\sigma S_e} = 1 : 1.49$, suggesting room for improvement of effective notch stress assessment is still left.

4. Conclusions and outlook

The fatigue lifetime of arc-welded joints is predominantly spent in the notch affected region, explaining why the effective notch stress S_e has been adopted as intact geometry fatigue strength parameter. A formulation has been established taking advantage of semi-analytical weld notch stress distribution expressions. Uniaxial mode-I and mode-III investigations [7,8,20] already revealed distinguished material dependent strength and mechanism contributions in terms of $\{\log(C), \gamma\}$ and $\{m, \rho^*\}$, i.e. respectively the resistance curve intercept and mean stress induced response ratio coefficient, resistance curve slope and material characteristic length. Since for mixed mode-{I, III} multiaxial response conditions of planar and tubular maritime structures the mode-I contribution is governing and at the same time the fatigue lifetime of arc-welded joints is growth defined rather than initiation controlled (i.e. a shear induced process) because of the welding induced defects, an equivalent normal stress based von Mises type of failure criterion at the critical fracture plane has been selected for fatigue assessment purposes. Cycles are counted in the von Mises plane, incorporating non-proportionality cycle-by-cycle and accumulating damage using a linear model.

In comparison to the assessment for other combinations of failure criterion, damage plane, cycle counting algorithm, non-proportionality measure and damage accumulation model in terms of lifetime and strength scatter; i.e. σ_N and $T_{\sigma S_e}$, the outperformance is impressive. Rather than a constant, a lifetime dependent shear strength coefficient $\beta(N)$ has been introduced to cover the mode specific and material characteristic $\{\log(C), m\}$, whereas S_e explicitly contains $\{\gamma, \rho^*\}$. The cycle-by-cycle non-proportionality measure includes a response path and material contribution. A 1st order response approach shows the best performance. Judgement is based on the affected data rather than all data, since balance between the non-proportional and other data does not exist. If non-proportionality involves a material aspect indeed seems impossible to prove, as the material fitting coefficient c_m behaves at the same time as a cycle counting and non-proportionality modelling deficiency correction factor. The multiaxial proportional data appears to show the largest scatter. However, the uniaxial mode-I and mode-III resistance (material) characteristics have been explicitly incorporated, as well as multiaxial mode-{I, III} non-proportionality measures, meaning that only for the multiaxial proportional data no specific resistance aspects have been considered; an obvious requirement to continue the improvement of the fatigue resistance formulation, for example incorporating a shear strength coefficient based on times series rather than a peak–valley sequence analysis – implying even the multiaxial proportional data would show non-proportional behaviour in the von Mises stress plane – or introducing coupling terms to the failure criterion.

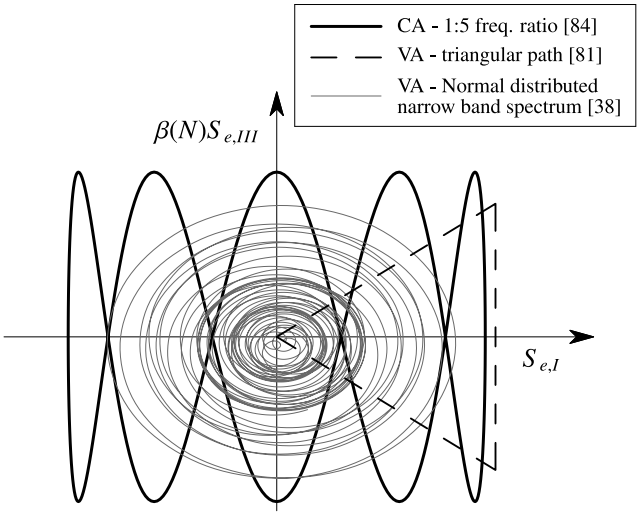

Fig. 24. Different stress histories in the von Mises stress plane.

The VA data fits the CA data scatter band for $D = 1$, supporting the hypothesis that an advanced fatigue strength parameter like S_e contributes to the (linear) damage accumulation model performance. However, most VA data involves a random sequence reflected in a Normal distributed narrow-band spectrum, meaning the data contains at maximum an averaged sequence effect. A response based non-linear damage model may still be required if data for different types of random sequence (e.g. broad-band spectra) or even for a determined sequence will be incorporated. A resistance induced non-linearity becomes relevant if both mid- and high-cycle fatigue become involved.

Although the obtained lifetime scatter parameter σ_N is still relatively large, the assessed uniaxial and multiaxial mode-{I, III} data fits the uniaxial mode-I reference data scatter band and a single $S_e - N$ resistance curve can be used for fatigue assessment in engineering applications. However, the aim for high accuracy may impose high engineer qualifications in order to satisfy the balance with model complexity and computational (programming) efforts.

CRediT authorship contribution statement

Gabriele Bufalari: Conceptualization, Methodology, Software, Validation, Formal analysis, Investigation, Data curation, Writing – original draft, Visualization. **Henk den Besten:** Conceptualization, Methodology, Writing – review & editing, Supervision. **Miroslaw Lech Kaminski:** Writing – review & editing, Supervision.

Declaration of competing interest

The authors declare that they have no known competing financial interests or personal relationships that could have appeared to influence the work reported in this paper.

Data availability

The fatigue resistance data used for model validation is available in literature.

Appendix. Effective notch stress formulations for symmetry with respect to $(t_p/2)$

Taking advantage of the stress distribution formulations for mode-I [61], the effective notch stress criterion $S_{e,I} = \Delta\sigma_e$ (Eq. 1) becomes in case of symmetry with respect to $(t_p/2)$ for $\rho = 0$:

$$
\begin{aligned}
S_{e,\mathrm{I}} = \Delta\sigma_s \left(\frac{t_p}{\rho_{\mathrm{I}}^*}\right) \Bigg\{ & \left[1 - 2r_{\sigma_s}\left(1 - f_{\rho=0}\left(\frac{r}{t_p} = \frac{1}{2}\right)\right)\right] \cdot \\
& \Bigg(\left(\frac{\rho_{\mathrm{I}}^*}{t_p}\right)^{\lambda_{\sigma s}} \frac{\mu_{\sigma s}\lambda_{\sigma s}(\lambda_{\sigma s}+1)}{\lambda_{\sigma s}} \left[\cos\{(\lambda_{\sigma s}+1)\beta_a\} - \chi_{\sigma s}\cos\{(\lambda_{\sigma s}-1)\beta_a\}\right] + \\
& \left(\frac{\rho_{\mathrm{I}}^*}{t_p}\right)^{\lambda_{\sigma a}} \frac{\mu_{\sigma a}\lambda_{\sigma a}(\lambda_{\sigma a}+1)}{\lambda_{\sigma a}} \left[\sin\{(\lambda_{\sigma a}+1)\beta_a\} - \chi_{\sigma a}\sin\{(\lambda_{\sigma a}-1)\beta_a\}\right] + \\
& C_{bw}\left\{2\left(\frac{\rho_{\mathrm{I}}^*}{t_p}\right)^2 - \left(\frac{\rho_{\mathrm{I}}^*}{t_p}\right)\right\}\Bigg) + r_{\sigma_s}\left\{2f_{\rho=0}\left(\frac{r}{t_p} = \frac{1}{2}\right) - 1\right\} \cdot \\
& \left[\left\{1 - f_{\rho=0}\left(\frac{r}{t_p} = \frac{1}{2}\right)\right\}\left(\frac{\rho_{\mathrm{I}}^*}{t_p}\right) - \left(\frac{\rho_{\mathrm{I}}^*}{t_p}\right)^2\right]\Bigg\}
\end{aligned}
\tag{A.1}
$$

with

$$
f_{\rho=0}\left(\frac{r}{t_p} = \frac{1}{2}\right) = \frac{(\lambda_{\sigma a} - \lambda_{\sigma s})(\lambda_{\sigma a}\lambda_{\sigma s} - 2C_{bw})}{\lambda_{\sigma a}(\lambda_{\sigma a} - 1) - \lambda_{\sigma s}(\lambda_{\sigma s} - 1)} + C_{bw}. \tag{A.2}
$$

For $\rho > 0$:

$$
\begin{aligned}
S_{e,\mathrm{I}} = \Delta\sigma_s \left(\frac{t_p}{r_0 + \rho_{\mathrm{I}}^*}\right) \Bigg\{ & \left[1 - 2r_{\sigma_s}\left(1 - f_{\rho>0}\left(\frac{r}{t_p} = \frac{1}{2}\right)\right)\right] \\
& \Bigg(\left[\left(\frac{r_0 + \rho_{\mathrm{I}}^*}{t_p}\right)^{\lambda_{\sigma s}} - \left(\frac{r_0}{t_p}\right)^{\lambda_{\sigma s}}\right] \frac{\mu_{\sigma s}\lambda_{\sigma s}(\lambda_{\sigma s}+1)}{\lambda_{\sigma s}} \cdot \\
& \left[\cos\{(\lambda_{\sigma s}+1)\beta_a\} - \chi_{\sigma s}\cos\{(\lambda_{\sigma s}-1)\beta_a\}\right] + \\
& \left[\left(\frac{r_0 + \rho_{\mathrm{I}}^*}{t_p}\right)^{\zeta_{\sigma s}} - \left(\frac{r_0}{t_p}\right)^{\zeta_{\sigma s}}\right]\left(\frac{r_0}{t_p}\right)^{\lambda_{\sigma s} - \zeta_{\sigma s}} \frac{\lambda_{\sigma s}}{\zeta_{\sigma s}} \frac{\left(\frac{2\alpha}{\pi}\right)}{4\left\{\left(\frac{2\alpha}{\pi}\right) - 1\right\}} \cdot \\
& \left[\omega_{\sigma s1}\cos\{(\zeta_{\sigma s}+1)\beta_a\} + \omega_{\sigma s2}(\zeta_{\sigma s}+1)\cos\{(\zeta_{\sigma s}-1)\beta_a\}\right] + \\
& \left[\left(\frac{r_0 + \rho_{\mathrm{I}}^*}{t_p}\right)^{\lambda_{\sigma a}} - \left(\frac{r_0}{t_p}\right)^{\lambda_{\sigma a}}\right] \frac{\mu_{\sigma a}\lambda_{\sigma a}(\lambda_{\sigma a}+1)}{\lambda_{\sigma a}} \cdot \\
& \left[\sin\{(\lambda_{\sigma a}+1)\beta_a\} - \chi_{\sigma a}\sin\{(\lambda_{\sigma a}-1)\beta_a\}\right] + \\
& \left[\left(\frac{r_0 + \rho_{\mathrm{I}}^*}{t_p}\right)^{\zeta_{\sigma a}} - \left(\frac{r_0}{t_p}\right)^{\zeta_{\sigma a}}\right]\left(\frac{r_0}{t_p}\right)^{\lambda_{\sigma a} - \zeta_{\sigma a}} \frac{\lambda_{\sigma a}}{4\zeta_{\sigma a}(\zeta_{\sigma a} - 1)} \cdot \\
& \left[\omega_{\sigma a1}\sin\{(\zeta_{\sigma a}+1)\beta_a\} + \omega_{\sigma a2}(\zeta_{\sigma a}+1)\sin\{(\zeta_{\sigma a}-1)\beta_a\}\right] + \\
& C_{bw}\left\{\left(\frac{r_0 + \rho_{\mathrm{I}}^*}{t_p}\right)^2 - \left(\frac{r_0}{t_p}\right)^2 - \left(\frac{2r_0 + \rho_{\mathrm{I}}^*}{t_p}\right)\right\}\Bigg) - r_{\sigma_s}\left\{2f_{\rho>0}\left(\frac{r}{t_p} = \frac{1}{2}\right) - 1\right\} \\
& \left[\left\{1 - f_{\rho>0}\left(\frac{r}{t_p} = \frac{1}{2}\right)\right\}\left(\frac{\rho_{\mathrm{I}}^*}{t_p}\right) - \left(\frac{\rho_{\mathrm{I}}^*}{t_p}\right)^2\right]\Bigg\}.
\end{aligned}
\tag{A.3}
$$

The mode-III effective notch stress criterion $S_{e,III} = \Delta\tau_e$ (Eq. 4) becomes in case of symmetry with respect to $(t_p/2)$ and $\rho = 0$ [20]:

$$
\begin{aligned}
S_{e,\mathrm{III}} = & \frac{2\Delta\tau_s}{\lambda_\tau}\left(\frac{t_p}{\rho_{\mathrm{III}}^*}\right)\Bigg\{\cos(\lambda_\tau\beta_a)\mu_{\tau F}\left(\frac{\rho_{\mathrm{III}}^*}{t_p}\right)^{\lambda_\tau}\left\{\frac{1}{2} + r_{\tau_s}\left[f_{\rho=0}\left(\frac{r}{t_p} = \frac{1}{2}\right) - 1\right]\right\} - \\
& \lambda_\tau\left(\frac{\rho_{\mathrm{III}}^*}{t_p}\right)\Bigg[\left(\frac{\rho_{\mathrm{III}}^*}{t_p}\right)\left\{\frac{\mu_{\tau M}}{2} + f_{\rho=0}\left(\frac{r}{t_p} = \frac{1}{2}\right) + C_{tw} - \frac{1}{2} + \right. \\
& \left.\left[f_{\rho=0}\left(\frac{r}{t_p} = \frac{1}{2}\right) - 1\right](\mu_{\tau M} + 2C_{tw})\, r_{\tau_s}\right\} - \\
& \left[f_{\rho=0}\left(\frac{r}{t_p} = \frac{1}{2}\right) - 1\right](\mu_{\tau M} + C_{tw})\, r_{\tau_s} + \left[f_{\rho=0}\left(\frac{r}{t_p} = \frac{1}{2}\right)\right]^2 - \\
& \frac{1}{2}\left[\mu_{\tau M} + 3f_{\rho=0}\left(\frac{r}{t_p} = \frac{1}{2}\right) + C_{tw} - 1\right]\Bigg]\Bigg\}
\end{aligned}
\tag{A.4}
$$

with

$$
f_{\rho=0}\left(\frac{r}{t_p} = \frac{1}{2}\right) = \left[\left(\frac{1}{2}\right)^{\lambda_\tau - 1}\mu_{\tau F}\cos(\lambda_\tau\beta_a) - C_{tw}\right]. \tag{A.5}
$$

For $\rho > 0$:

$$
\begin{aligned}
S_{e,\mathrm{III}} = & \frac{2\Delta\tau_s}{\lambda_\tau}\left(\frac{t_p}{r_0 + \rho_{\mathrm{III}}^*}\right)\Bigg\langle\left[\cos(\lambda_\tau\beta_a)\mu_{\tau F}\left\{\frac{1}{2} + \left[f_{\rho>0}\left(\frac{r}{t_p} = \frac{1}{2}\right) - 1\right]r_{\tau_s}\right\}\right] \cdot \\
& \left\{\left(\frac{r_0}{t_p}\right)^{2\lambda_\tau}\left[\left(\frac{r_0}{t_p}\right)^{-\lambda_\tau} - \left(\frac{r_0 + \rho_{\mathrm{III}}^*}{t_p}\right)^{-\lambda_\tau}\right] - \right. \\
& \left.\left[\left(\frac{r_0}{t_p}\right)^{\lambda_\tau} - \left(\frac{r_0 + \rho_{\mathrm{III}}^*}{t_p}\right)^{\lambda_\tau}\right]\right\} - \lambda_\tau\frac{\rho_{\mathrm{III}}^*}{t_p}\left\{r_{\tau_s}\left[f_{\rho>0}\left(\frac{r}{t_p} = \frac{1}{2}\right) - 1\right] \cdot \right. \\
& \left[(\mu_{\tau M} + 2C_{tw})\left(\frac{2r_0 + \rho_{\mathrm{III}}^*}{t_p}\right) - \mu_{\tau M} - C_{tw}\right] + \\
& \left(\frac{\rho_{\mathrm{III}}^*}{t_p}\right)\left[\frac{\mu_{\tau M}}{2} + C_{tw} + f_{\rho>0}\left(\frac{r}{t_p} = \frac{1}{2}\right) - \frac{1}{2}\right] + \\
& \left[f_{\rho>0}\left(\frac{r}{t_p} = \frac{1}{2}\right)\right]^2 + \left[\left(\frac{r_0}{t_p}\right) - \frac{3}{2}\right]f_{\rho>0}\left(\frac{r}{t_p} = \frac{1}{2}\right) + \\
& \left.\left(\frac{\mu_{\tau M}}{2} + C_{tw} - \frac{1}{2}\right)\left(\frac{r_0}{t_p}\right) + \frac{1}{2} - \frac{\mu_{\tau M}}{2} - \frac{C_{tw}}{2}\right\}\Bigg\rangle
\end{aligned}
\tag{A.6}
$$

with

$$f_{\rho>0}\left(\frac{r}{t_p}=\frac{1}{2}\right)=\Bigg[\left(\frac{2r_0+1}{2t_p}\right)^{\lambda_\tau-1}\mu_{\tau F}\cos(\lambda_\tau\beta_a)\cdot\left\{\left(\frac{2r_0+1}{2t_p}\right)^{-2\lambda_\tau}\left(\frac{r_0}{t_p}\right)^{2\lambda_\tau}+1\right\}-\mu_{\tau M}\left\{2\left(\frac{2r_0+1}{2t_p}\right)-1\right\}-C_{tw}\left\{4\left(\frac{2r_0+1}{2t_p}\right)-1\right\}\Bigg]. \tag{A.7}$$

References

[1] Schijve J. Fatigue of structures and materials. Springer Netherlands; 2009.

[2] Den Besten J. Fatigue damage criteria classification, modelling developments and trends for welded joints in marine structures. Ships Offshore Struct 2018;13:787–808. http://dx.doi.org/10.1080/17445302.2018.1463609.

[3] Van Lieshout PS, Den Besten JH, Kaminski ML. Multiaxial fatigue assessment of welded joints in marine structures: Literature overview of progress in academia and engineering practice. Int Shipbuild Prog 2018;65:29–71. http://dx.doi.org/10.3233/ISP-170141.

[4] Glen I, Dinovitzer A, Paterson R, Luznik L, Bayley C. Fatigue resistant detail design guide for ship structures - Ship Structure Committee. U.S. Coast Guard Headquarters; 1999.

[5] Guedes Soares C, Garbatov Y. Proceedings of 19th international ship and offshore structures congress (ISSC 2015). Mar Struct 2015;74. http://dx.doi.org/10.1016/j.marstruc.2017.09.001.

[6] Lassen T, Recho N. Proposal for a more accurate physically based S-N curve for welded steel joints. Int J Fatigue 2009;31:70–8. http://dx.doi.org/10.1016/j.ijfatigue.2008.03.032.

[7] Qin Y, Den Besten J, Palkar S, Kaminski ML. Mid- and high-cycle fatigue of welded joints in steel marine structures: Effective notch stress and total stress concept evaluations. Int J Fatigue 2021;142:105822. http://dx.doi.org/10.1016/j.ijfatigue.2020.105822.

[8] Qin Y, Den Besten J, Palkar S, Kaminski ML. Fatigue design of welded double-sided T-joints and double-sided cruciform joints in steel marine structures: A total stress concept. Fatigue Fract Eng Mater Struct 2019;42:2674–93. http://dx.doi.org/10.1111/ffe.13089.

[9] Neuber H. Kerbspannungslehre. Springer - Verlag; 1937.

[10] Zhang G, Sonsino CM, Sundermeier R. Method of effective stress for fatigue: Part II – Applications to V-notches and seam welds. Int J Fatigue 2012;37:24–40. http://dx.doi.org/10.1016/j.ijfatigue.2011.09.016.

[11] Sonsino CM, Fricke W, De Bruyne F, Hoppe A, Ahmadi A, Zhang G. Notch stress concepts for the fatigue assessment of welded joints - Background and applications. Int J Fatigue 2012;34:2–16. http://dx.doi.org/10.1016/j.ijfatigue.2010.04.011.

[12] Radaj D, Lazzarin P, Berto F. Generalised Neuber concept of fictitious notch rounding. Int J Fatigue 2013;51:105–15. http://dx.doi.org/10.1016/j.ijfatigue.2013.01.005.

[13] Carpinteri A, Boaretto J, Fortese G, Giordani F, Iturrioz I, Ronchei C, Scorza D, Vantadori S. Fatigue life estimation of fillet-welded tubular T-joints subjected to multiaxial loading. Int J Fatigue 2017;101:263–70. http://dx.doi.org/10.1016/j.ijfatigue.2016.10.012.

[14] Vantadori S, Iturrioz I, Carpinteri A, Greco F, Ronchei C. A novel procedure for damage evaluation of fillet-welded joints. Int J Fatigue 2020;136. http://dx.doi.org/10.1016/j.ijfatigue.2020.105599.

[15] Taylor D. The theory of critical distances. Elsevier Science & Technology; 2014.

[16] Ezeh O, Susmel L. On the notch fatigue strength of additively manufactured polylactide (PLA). Int J Fatigue 2020;136:105583. http://dx.doi.org/10.1016/j.ijfatigue.2020.105583.

[17] Gillham B, Yankin A, McNamara F, Tomonto C, Taylor D, Lupoi R. Application of the Theory of Critical Distances to predict the effect of induced and process inherent defects for SLM Ti-6Al-4V in high cycle fatigue. CIRP Ann 2021;70(1):171–4. http://dx.doi.org/10.1016/j.cirp.2021.03.004.

[18] Gillham B, Yankin A, McNamara F, Tomonto C, Huang C, Soete J, O'Donnell G, Trimble D, Yin S, Taylor D, Lupoi R. Tailoring the theory of critical distances to better assess the combined effect of complex geometries and process-inherent defects during the fatigue assessment of SLM Ti-6Al-4V. Int J Fatigue 2023;172:107602. http://dx.doi.org/10.1016/j.ijfatigue.2023.107602.

[19] Bartsch H, Citarelli S, Feldmann M. Generalisation of the effective notch stress concept for the fatigue assessment of arbitrary steel structures. J Constr Steel Res 2023;201:107715. http://dx.doi.org/10.1016/j.jcsr.2022.107715.

[20] Bufalari G, Den Besten JH, Kaminski ML. Mode-III fatigue of welded joints in steel maritime structures: Weld notch shear stress distributions and effective notch stress based resistance. Int J Fatigue 2022;107210. http://dx.doi.org/10.1016/J.IJFATIGUE.2022.107210.

[21] Pedersen MM. Multiaxial fatigue assessment of welded joints using the notch stress approach. Int J Fatigue 2016;83:269–79. http://dx.doi.org/10.1016/j.ijfatigue.2015.10.021.

[22] Larsen ML, Baumgartner J, Clausen HB, Arora V. Multiaxial fatigue assessment of welded joints using a principal component-based measure for non-proportionality. Int J Fatigue 2022;158. http://dx.doi.org/10.1016/j.ijfatigue.2022.106731.

[23] Fatemi A, Shamsaei N. Multiaxial fatigue: An overview and some approximation models for life estimation. Int J Fatigue 2011;33:948–58. http://dx.doi.org/10.1016/j.ijfatigue.2011.01.003.

[24] Hibbeler R, Yap K. Mechanics of materials. Pearson; 2018.

[25] Papuga J, Růžička M. Two new multiaxial criteria for high cycle fatigue computation. Int J Fatigue 2008;30:58–66. http://dx.doi.org/10.1016/J.IJFATIGUE.2007.02.015.

[26] Papuga J. A survey on evaluating the fatigue limit under multiaxial loading. Int J Fatigue 2011;33:153–65. http://dx.doi.org/10.1016/j.ijfatigue.2010.08.001.

[27] Papuga J, Nesládek M, Kuželka J, Jurenka J. Differences in the response to in-phase and out-of-phase multiaxial high-cycle fatigue loading. Frattura Integr Strutt 2019;13:163–83. http://dx.doi.org/10.3221/IGF-ESIS.50.15.

[28] Carpinteri A, Spagnoli A, Vantadori S, Bagni C. Structural integrity assessment of metallic components under multiaxial fatigue: The C-S criterion and its evolution. Fatigue Fract Eng Mater Struct 2013;36:870–83. http://dx.doi.org/10.1111/ffe.12037.

[29] Susmel L. A simple and efficient numerical algorithm to determine the orientation of the critical plane in multiaxial fatigue problems. Int J Fatigue 2010;32:1875–83. http://dx.doi.org/10.1016/J.IJFATIGUE.2010.05.004.

[30] Susmel L, Askes H. Modified Wöhler Curve Method and multiaxial fatigue assessment of thin welded joints. Int J Fatigue 2012;43:30–42. http://dx.doi.org/10.1016/j.ijfatigue.2012.01.026.

[31] Susmel L. Four stress analysis strategies to use the Modified Wöhler Curve Method to perform the fatigue assessment of weldments subjected to constant and variable amplitude multiaxial fatigue loading. Int J Fatigue 2014;67:38–54. http://dx.doi.org/10.1016/j.ijfatigue.2013.12.001.

[32] Susmel L, Taylor D. The modified Wöhler curve method applied along with the theory of critical distances to estimate finite life of notched components subjected to complex multiaxial loading paths. Fatigue Fract Eng Mater Struct 2008;31:1047–64. http://dx.doi.org/10.1111/j.1460-2695.2008.01296.x.

[33] Anes V, Reis L, Li B, Fonte M, De Freitas M. New approach for analysis of complex multiaxial loading paths. Int J Fatigue 2014;62:21–33. http://dx.doi.org/10.1016/j.ijfatigue.2013.05.004.

[34] Dong P, Wei Z, Hong JK. A path-dependent cycle counting method for variable-amplitude multi-axial loading. Int J Fatigue 2010;32:720–34. http://dx.doi.org/10.1016/j.ijfatigue.2009.10.010.

[35] Wei Z, Dong P, Mei J, Pei X, Ravi SK. A moment of load path-based parameter for modeling multiaxial fatigue damage of welded structures. Int J Fatigue 2023;171:107575. http://dx.doi.org/10.1016/J.IJFATIGUE.2023.107575.

[36] Kim J-S, Kim C, Jin T-E, Dong P. Mean load effect on fatigue of welded joints using structural stress and fracture mechanics approach. Nucl Eng Technol 2006;38.

[37] Sonsino CM. Multiaxial fatigue of welded joints under in-phase and out-of-phase local strains and stresses. Int J Fatigue 1995;17:55–70. http://dx.doi.org/10.1016/0142-1123(95)93051-3.

[38] Sonsino CM, Kueppers M. Multiaxial fatigue of welded joints under constant and variable amplitude loadings. Fatigue Fract Eng Mater Struct 2001;24:309–27. http://dx.doi.org/10.1046/j.1460-2695.2001.00393.x.

[39] Bolchoun A, Sonsino CM, Kaufmann H, Melz T. Multiaxial random fatigue of magnesium laserbeam-welded joints-Experimental results and numerical fatigue life evaluation. In: Procedia engineering, Vol. 101. Elsevier Ltd; 2015, p. 61–8. http://dx.doi.org/10.1016/j.proeng.2015.02.009.

[40] Papadopoulos IV, Davoli P, Gorla C, Filippini M, Bernasconi A. A comparative study of multiaxial high-cycle fatigue criteria for metals. Int J Fatigue 1997;19:219–35. http://dx.doi.org/10.1016/S0142-1123(96)00064-3.

[41] Meggiolaro MA, De Castro JTP. An improved multiaxial rainflow algorithm for non-proportional stress or strain histories - Part I: Enclosing surface methods. Int J Fatigue 2012;42:217–26. http://dx.doi.org/10.1016/j.ijfatigue.2011.10.014.

[42] Jiang C, Liu ZC, Wang XG, Zhang Z, Long XY. A structural stress-based critical plane method for multiaxial fatigue life estimation in welded joints. Fatigue Fract Eng Mater Struct 2016;39:372–83. http://dx.doi.org/10.1111/FFE.12369.

[43] Cristofori A, Susmel L, Tovo R. A stress invariant based criterion to estimate fatigue damage under multiaxial loading. Int J Fatigue 2008;30:1646–58. http://dx.doi.org/10.1016/j.ijfatigue.2007.11.006.

[44] Anes V, Reis L, Li B, De Freitas M. New cycle counting method for multiaxial fatigue. Int J Fatigue 2014;67:78–94. http://dx.doi.org/10.1016/j.ijfatigue.2014.02.010.

[45] Bishop N, Sherratt F. Finite element based fatigue calculations. NAFEMS; 2000, http://dx.doi.org/10.59972/TA5H05JD.

[46] Papuga J, Vargas M, Hronek M. Evaluation of uniaxial fatigue criteria applied to multiaxially loaded unnotched samples. Eng Mech 2012;19:99–111.

[47] Carpinteri A, Spagnoli A, Vantadori S. A multiaxial fatigue criterion for random loading. Fatigue Fract Eng Mater Struct 2003;26:515–22. http://dx.doi.org/10.1046/j.1460-2695.2003.00620.x.

[48] Wang CH, Brown MW. Life prediction techniques for variable amplitude multiaxial fatigue — Part 1 : Theories. Eng Mater Technol 1996;118:367–70.

[49] Meggiolaro MA, De Castro JTP. An improved multiaxial rainflow algorithm for non-proportional stress or strain histories - Part II: The Modified Wang-Brown method. Int J Fatigue 2012;42:194–206. http://dx.doi.org/10.1016/j.ijfatigue.2011.10.012.

[50] Mei J, Dong P. A new path-dependent fatigue damage model for non-proportional multi-axial loading. Int J Fatigue 2016;90:210–21. http://dx.doi.org/10.1016/j.ijfatigue.2016.05.010.

[51] Fatemi A, Yang L. Cumulative fatigue damage and life prediction theories: a survey of the state of the art for homogeneous materials. Int J Fatigue 1998;20:9–34. http://dx.doi.org/10.1016/S0142-1123(97)00081-9.

[52] Hectors K, De Waele W. Cumulative damage and life prediction models for high-cycle fatigue of metals: A review. Metals 2021;11:1–32. http://dx.doi.org/10.3390/met11020204.

[53] Palmgren A. Die lebensdauer von kugellagern (life length of roller bearings or durability of ball bearings). Z Vereines Dtsch Ing 1924;14:339–41.

[54] Miner MA. Cumulative damage in fatigue. J Appl Mech 1945;12:A159–64. http://dx.doi.org/10.1115/1.4009458.

[55] Deul M. Fatigue damage accumulation in steel welded joints, subject to (random) variable amplitude loading conditions: An improved fatigue-life model for naval ship structural design (MSc. thesis), Delft University of Technology; 2021.

[56] Fricke W, Paetzold H. Effect of whipping stresses on the fatigue damage of ship structures. Weld World 2014;58:261–8. http://dx.doi.org/10.1007/s40194-014-0111-5.

[57] Gurney TR. Cumulative damage of welded joints. Woodhead Publishing; 2006, p. 442.

[58] Sonsino CM, Łagoda T. Assessment of multiaxial fatigue behaviour of welded joints under combined bending and torsion by application of a fictitious notch radius. Int J Fatigue 2004;26:265–79. http://dx.doi.org/10.1016/S0142-1123(03)00143-9.

[59] Agerskov H. Fatigue in steel structures under random loading. J Constr Steel Res 2000;53:283–305. http://dx.doi.org/10.1016/S0143-974X(99)00042-5.

[60] Xi L, Songlin Z. Strengthening and damaging under low-amplitude loads below the fatigue limit. Int J Fatigue 2009;31:341–5. http://dx.doi.org/10.1016/j.ijfatigue.2008.08.004.

[61] Den Besten J. Fatigue resistance of welded joints in aluminium high-speed craft: a total stress concept (Ph.D. thesis), Delft University of Technology; 2015.

[62] Haibach E. The allowable stresses under variable amplitude loading of welded joints. In: Proceedings of the conference of the fatigue welded structures, Vol. 2. Cambridgeshire South East, UK: The Welding Institute; 1971, p. 328–39.

[63] Sonsino CM, Łagoda T, Demofonti G. Damage accumulation under variable amplitude loading of welded medium- and high-strength steels. Int J Fatigue 2004;26:487–95. http://dx.doi.org/10.1016/j.ijfatigue.2003.10.001.

[64] Leonetti D, Maljaars J, Snijder HH. Fitting fatigue test data with a novel S-N curve using frequentist and Bayesian inference. Int J Fatigue 2017;105:128–43. http://dx.doi.org/10.1016/J.IJFATIGUE.2017.08.024.

[65] DNV-GL. Fatigue assessment of ship structures. Classification note 30.7. DNV-GL; 2014.

[66] Gough HJ, Pollard HV. The strength of metals under combined alternating stresses. Proc Int Mech Eng 1935;131:3–103.

[67] Hobbacher AF. Recommendations for fatigue design of welded joints and components. IIW collection, Springer International; 2016.

[68] Sonsino CM. Multiaxial fatigue assessment of welded joints - Recommendations for design codes. Int J Fatigue 2009;31:173–87. http://dx.doi.org/10.1016/j.ijfatigue.2008.06.001.

[69] Crossland B. Effect of large hydrostatic stress on the torsional fatigue strength of an alloy steel. In: International conference on fatigue of metals. London; 1956, p. 138–49.

[70] Dong P. A structural stress definition and numerical implementation for fatigue analysis of welded joints. Int J Fatigue 2001;23:865–76. http://dx.doi.org/10.1016/S0142-1123(01)00055-X.

[71] Dong P, Hong JK. The master S-N curve approach to fatigue evaluation of offshore and marine structures. In: 23rd international conference on offshore mechanics and arctic engineering, Volume 2. 2004, p. 847–55.

[72] Dong P. A robust structural stress method for fatigue analysis of ship structures. In: Proceedings of the international conference on offshore mechanics and arctic engineering - OMAE, Vol. 3. American Society of Mechanical Engineers Digital Collection; 2003, p. 199–211. http://dx.doi.org/10.1115/OMAE2003-37313.

[73] CEN. EN 1993-1-9: Eurocode 3: Design of steel structures - Part 1-9: Fatigue. The European Union; 2005.

[74] DNV. RP-C203: Fatigue design of offshore steel structures. Recommended Practice DNV-RPC203, 2014, p. 126.

[75] Rodrigues DM, Leitão C, Balakrishnan M, Craveiro HD, Santiago A. Tensile properties of S355 butt welds after exposure to high temperatures. Constr Build Mater 2021;302:124374. http://dx.doi.org/10.1016/J.CONBUILDMAT.2021.124374.

[76] Konat L, Białobrzeska B. Effect of welding technique and thermal treatment parameters on abrasive wear of steel S355. Tribologia 2022;301:25–38. http://dx.doi.org/10.5604/01.3001.0016.1021.

[77] Pandey C, Giri A, Mahapatra MM, Kumar P. Characterization of microstructure of HAZs in as-welded and service condition of P91 pipe weldments. Met Mater Int 2017;23:148–62. http://dx.doi.org/10.1007/s12540-017-6394-5.

[78] De Jesus AM, Matos R, Fontoura BF, Rebelo C, Da Silva LS, Veljkovic M. A comparison of the fatigue behavior between S355 and S690 steel grades. J Constr Steel Res 2012;79:140–50. http://dx.doi.org/10.1016/J.JCSR.2012.07.021.

[79] Yousefi F, Witt M, Zenner H. Fatigue strength of welded joints under multiaxial loading: Experiments and calculations. Fatigue Fract Eng Mater Struct 2001;24:339–55. http://dx.doi.org/10.1046/j.1460-2695.2001.00397.x.

[80] Siljander A, Kurath P, Lawrence FV. Non proportional fatigue of welded structures. ASTM Spec Tech Publ 1992;319–38. http://dx.doi.org/10.1520/stp24166s.

[81] Witt M, Zenner H. Multiaxial fatigue behavior of welded flange-tube connections under combined loading. Experiments and lifetime prediction. In: 5th international conference on biaxial/multiaxial fatigue & fracture. I. 1997, p. 421–34.

[82] Seeger T, Olivier R. Ertragbare und zulassige schubspannungen schwingbeanspruchter schweissverbindungen. Stahlbau 1987.

[83] Amstutz H, Störzel K, Seeger T. Fatigue crack growth of a welded tube-flange connection under bending and torsional loading. Fatigue Fract Eng Mater Struct 2001;24:357–68. http://dx.doi.org/10.1046/j.1460-2695.2001.00408.x.

[84] Razmjoo GR. Fatigue of load-carrying fillet welded joints under multiaxial loading. In: Fatigue – Core research from TWI. Woodhead, UK: European Structural Integrity Society; 2000, p. 63–99.

[85] Yung, Lawrence F. Predicting the fatigue life of welds under combined bending and torsion. In: Biaxial and multiaxial fatigue. Mechanical Engineering Publications; 1986, p. 53–69.

[86] Meneghetti G, Campagnolo A, Babini V, Riboli M, Spagnoli A. Multiaxial fatigue assessment of welded steel details according to the peak stress method: Industrial case studies. Int J Fatigue 2019;125:362–80. http://dx.doi.org/10.1016/j.ijfatigue.2019.04.014.

[87] Bäckström M. Multiaxial fatigue life assessment of welds based on nominal and hot spot stresses (Ph.D. thesis), Finland: Laapeenranta University; 2003.

[88] Archer R. Fatigue of a welded steel attachment under combined direct stress and shear stress. In: International conference of fatigue of welded constructions. Brighton, England; 1987, p. 63–72.

[89] Dahle T, Olsson KE, Samuelsson J. Fatigue design optimisation of welded box beams subjected to combined bending and torsion. Eur Struct Integr Soc 1999;23:103–16. http://dx.doi.org/10.1016/S1566-1369(99)80034-X.

[90] Takahashi I, Takada A, Ushijima M, Akiyama S. Fatigue behaviour of a box-welded joint under biaxial cyclic loading: Effects of biaxial load range ratio and cyclic compressive loads in the lateral direction. Fatigue Fract Eng Mater Struct 2003;26:439–48. http://dx.doi.org/10.1046/j.1460-2695.2003.00645.x.

[91] Maddox SJ. Fatigue assessment of welds not oriented either normal or parallel to the direction of loading. IIW Document J WG XIII/ XV-218-10, 2010.

[92] Kim I, Yamada K. Fatigue behaviour of fillet welded joints inclined to a uniaxial cyclic load. IIW Document XIII-2021-04, 2004.

[93] Dekking FM, Kraaikamp C, Lopuhaä HP, Meester LE. A modern introduction to probability and statistics: Understanding why and how. Springer - Verlag London; 2005, http://dx.doi.org/10.1198/tech.2007.s502.

[94] Qin Y, Den Besten J, Kaminski ML. Weld toe and weld root notch induced fatigue of welded joints in steelmarine structures: effective notch stress and total stress concept evaluations. Int J Fatigue 2024. (in preparation).

[95] Mei J, Dong P, Xing S, Vasu A, Ganamet A, Chung J, Mehta Y. An overview and comparative assessment of approaches to multi-axial fatigue of welded components in codes and standards. Int J Fatigue 2021;146:106144. http://dx.doi.org/10.1016/j.ijfatigue.2021.106144.

[96] Fonte M, Reis L, Romeiro F, Li B, De Freitas M. The effect of steady torsion on fatigue crack growth in shafts. Int J Fatigue 2006;28:609–17. http://dx.doi.org/10.1016/J.IJFATIGUE.2005.06.051.

[97] Hong JK, Forte TP. Fatigue evaluation procedures for multiaxial loading in welded structures using battelle structural stress approach. In: Proceedings of the international conference on offshore mechanics and arctic engineering - OMAE, Vol. 5. American Society of Mechanical Engineers Digital Collection; 2014, http://dx.doi.org/10.1115/OMAE2014-23459.

[98] Susmel L, Lazzarin P. A bi-parametric Wöhler curve for high cycle multiaxial fatigue assessment. Fatigue Fract Eng Mater Struct 2002;25:63–78. http://dx.doi.org/10.1046/J.1460-2695.2002.00462.X.